

MASTERARBEIT IN PHYSIK

**Low-Energy Dispersive Analysis of the  
Electromagnetic Kaon Form Factors**

---

von  
Deepti Hariharan


angefertigt im  
*Helmholtz-Institut für Strahlen- und Kernphysik*

vorgelegt der  
*Mathematisch-Naturwissenschaftlichen Fakultät der  
Rheinischen Friedrich-Wilhelms-Universität  
Bonn*

---

October 2021

I hereby declare that the work presented here was formulated by myself and no sources and tools other than those cited were used.

Bonn, 02-10-2021 signature 

1. Gutachter:

PD Dr. Bastian Kubis  
Helmholtz-Institut für Strahlen- und Kernphysik  
Universität Bonn

2. Gutachter:

Prof. Dr. Christoph Hanhart  
Institut für Kernphysik  
Forschungszentrum Jülich

## Abstract

A model for the electromagnetic form factors of kaons is presented. The calculation of the kaon form factor has implications in the theoretical determination of the anomalous magnetic moment of the muon. The isovector part of the form factor is calculated employing the dispersion method for the process of a virtual photon decaying into a pair of kaons via a two-pion intermediate state. The isoscalar part is found to follow the vector meson dominance model with the Breit-Wigner formalism. This model is then tested phenomenologically with numerous datasets in the timelike region, and also in combination with data from the spacelike region. The  $SU(3)$  coupling of the  $\phi(1020)$  and  $\omega(782)$  resonance states have been determined from the fits in addition to the  $\phi$ -meson mass and width.

# Contents

|          |   |           |
|----------|---|-----------|
| <b>1</b> | <b>Introduction</b>                                 | <b>1</b>  |
| <b>2</b> | <b>Dispersion Relations</b>                         | <b>5</b>  |
| 2.1      | Unitarity . . . . .                                 | 5         |
| 2.2      | Analyticity . . . . .                               | 6         |
| 2.3      | Pion Vector Form Factor . . . . .                   | 9         |
| 2.3.1    | Watson's Final State Theorem . . . . .              | 9         |
| 2.3.2    | Omnès Solution . . . . .                            | 11        |
| 2.3.3    | Computation of Pion Vector Form Factor . . . . .    | 11        |
| <b>3</b> | <b>Isovector Part of the Kaon Form Factor</b>       | <b>14</b> |
| 3.1      | Calculation of the Imaginary Part . . . . .         | 14        |
| 3.2      | Computing Full Isovector Kaon Form Factor . . . . . | 16        |
| 3.3      | Comparison with BaBar Data . . . . .                | 17        |
| <b>4</b> | <b>Isoscalar Part of the Kaon Form Factor</b>       | <b>20</b> |
| 4.1      | $\gamma V$ Vertex . . . . .                         | 21        |
| 4.2      | $V\Phi\Phi$ Vertex . . . . .                        | 23        |
| 4.3      | Full Diagram . . . . .                              | 24        |
| <b>5</b> | <b>Phenomenology</b>                                | <b>27</b> |
| 5.1      | Experimental Datasets . . . . .                     | 27        |
| 5.2      | Fits . . . . .                                      | 30        |
| 5.3      | Observations . . . . .                              | 31        |
| <b>6</b> | <b>Summary</b>                                      | <b>42</b> |
| <b>A</b> | <b>Kinematics</b>                                   | <b>44</b> |
| <b>B</b> | <b>Fits</b>   | <b>47</b> |
|          | <b>Bibliography</b>                                 | <b>49</b> |

# Chapter 1

## Introduction

The standard model (SM) of particle physics explains the basic interactions of particle physics in terms of the  $U(1) \times SU(2) \times SU(3)$  non-abelian gauge groups [1]. The  $U(1) \times SU(2)$  gauge group describes the electroweak interactions, while the  $SU(3)$  group describes the quantum chromodynamics (QCD) aspect.

QCD describes the strong interaction between quarks and gluons. The QCD coupling decreases asymptotically with increasing energy. At short range, quarks rapidly exchange gluons creating a colour force which increases with distance between the quarks. This field confines the quarks and gluons into colour-neutral hadrons.

The determination of the magnetic moment of leptons is an important test for the standard model of particle physics. The magnetic moment is defined as

$$\vec{\mu}_l = g_l \left( \frac{q}{2M_l} \right) \vec{s}, \quad (1.1)$$

where  $g_l$  is the  $g$ -factor of the lepton,  $M_l, q$  its mass and charge, and  $\vec{s}$  is the spin angular momentum. The Dirac equation predicts  $g = 2$  [2]. The anomalous magnetic moment is defined as

$$a = \frac{g - 2}{2}. \quad (1.2)$$

In 1948, Schwinger calculated an additional contribution to the magnetic moment from radiative corrections,  $a = \alpha/2\pi \approx 0.00116$  [3], which agrees with experiments up to three significant digits.

The contributions to the anomalous magnetic moment of the muon includes electromagnetic, weak and strong interactions. First-principle calculations of the hadronic contribution are hard and do not give reliable results. Therefore, the uncertainty in  $a_\mu$  is fully dominated by hadronic processes, such as the hadronic vacuum polarization (HVP) and the hadronic light-by-light (HLbL) scattering as shown in fig. 1.1. HVP is the second largest contribution to the uncertainty of  $a_\mu$  [4]. The most recent experimental determination of the anomalous muon magnetic moment was done at the Fermi National Accelerator Laboratory (FNAL) [5]. The average result of FNAL and Brookhaven National Laboratory (BNL) [6] was found to be

$$a_{\mu(\text{Exp})} = 116592061(41) \times 10^{-11},$$

and the theoretical value calculated so far is [4]

$$a_{\mu(\text{Th})} = 116591810.8(37.8) \times 10^{-11}.$$

The difference between the experimental average and the theoretical estimation is  $4.2\sigma$ . The graphical representation is shown in fig. 1.2. This is one of the few places where persistent tensions with experiments are observed in the standard model.

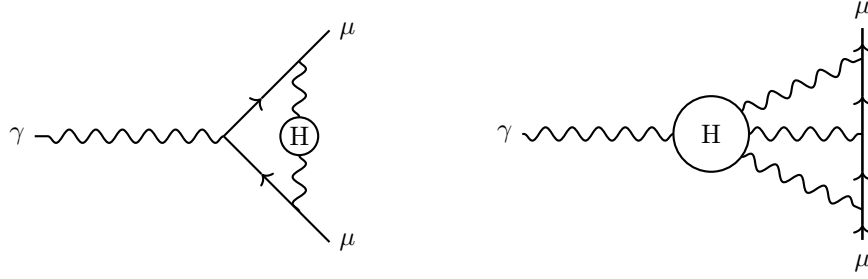


Figure 1.1: Contributions to muon anomalous magnetic moment.

The diagram on the left shows the contribution of the hadronic vacuum polarisation and the diagram on the right shows the contribution of hadronic light-by-light scattering.

One contribution to the hadronic vacuum polarization of the muon is from the spontaneous production and decay of pseudoscalars such as the kaon. Charged kaons also contribute to  $a_\mu$  via the kaon box diagram in HLbL, which depends primarily on the spacelike kaon form factor. The diagrams for the HVP and HLbL contributions are shown in fig. 1.3. These contributions can be calculated by determining the form factor of the particle.

## Kaon Contribution

The kaon is a type of meson (two-quark system) that consists of a strange quark in combination with an up or down quark;  $K^+ : u\bar{s}$ ,  $K^- : s\bar{u}$ ,  $K^0 : d\bar{s}$ ,  $\bar{K}^0 : s\bar{d}$ . The neutral kaons can further mix into the short- and long-lived states denoted by  $K_S$  and  $K_L$ , respectively. These are the physical eigenstates in which neutral kaons are observed, given by

$$\begin{aligned} |K_S\rangle &= \frac{1}{\sqrt{2}}(|K^0\rangle + |\bar{K}^0\rangle), \\ |K_L\rangle &= \frac{1}{\sqrt{2}}(|K^0\rangle - |\bar{K}^0\rangle). \end{aligned} \tag{1.3}$$

Kaons play a major role in understanding the fundamental interactions and symmetry violations in the standard model of particle physics. Certain kaon decays violate CP symmetry, which can potentially explain the matter-antimatter asymmetry in the universe. Kaons can contribute to the understanding of the anomalous magnetic moment of the muon in the hadronic sector.

A general diagram for the kaon form factor is shown in fig. 1.4. Previous calculations and measurements of the kaon form factor used the vector meson dominance (VMD) model to determine the major resonances [7]. There are very few explicit dispersive calculations of the isovector part of the form factor dominated by the  $\rho$ -meson. One theoretical calculation of the  $\rho$  contribution was done by a once-subtracted dispersion relation in [8]. In this work, we calculate the isovector part of the form factor using an unsubtracted dispersion relation. The isoscalar part is calculated using the Lagrangian from [9], which ultimately leads to an approximation of the  $SU(3)$ -symmetric VMD model.

The full form factor is a linear combination of the isoscalar  $F_K^S(s)$  and isovector  $F_K^V(s)$  channels

$$F_{K^{\pm,0}}(s) = F_K^S(s) \pm F_K^V(s), \tag{1.4}$$

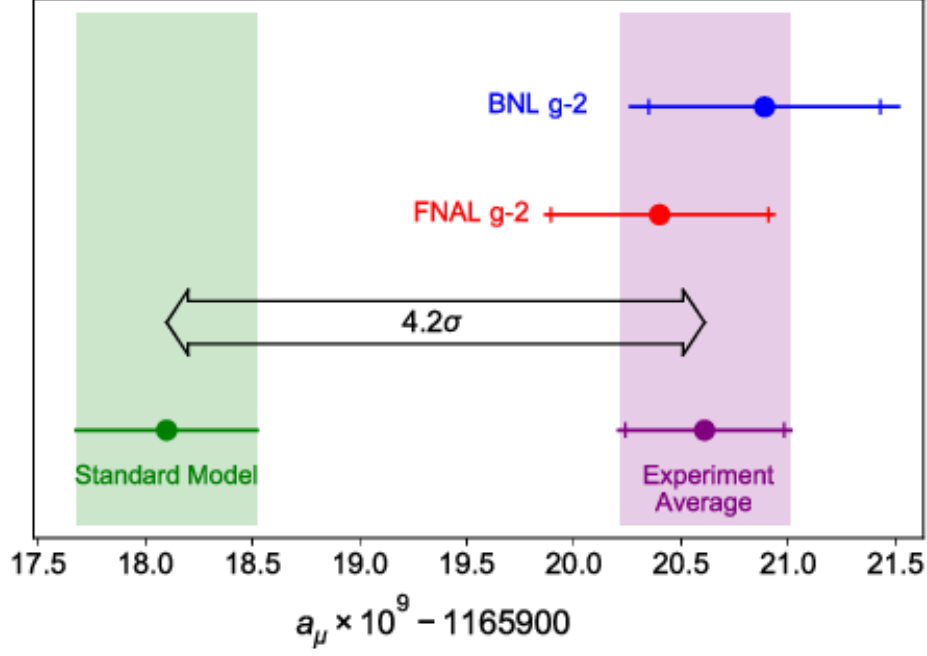


Figure 1.2: Comparison of experimental results and theoretical average of  $a_\mu$  taken from [5].

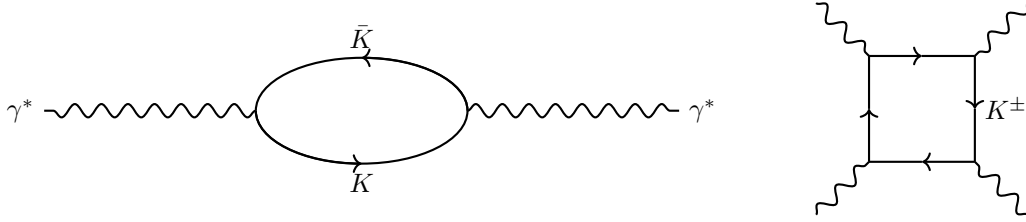


Figure 1.3: Kaon contribution to muon  $g - 2$ .

The first diagram on the left shows the kaon loop contribution to HVP and the second diagram shows the HLbL contribution of charged kaons.

with the normalisation as follows

$$\begin{aligned}
 F_K^S(0) &= F_K^V(0) = \frac{1}{2}, \\
 F_{K^+}(0) &= F_K^S(0) + F_K^V(0) = 1, \\
 F_{K^0}(0) &= F_K^S(0) - F_K^V(0) = 0.
 \end{aligned}
 \tag{1.5}$$

We then fit the theoretical model of the form factor to data in both the timelike region around the  $\phi(1020)$ -meson, and the spacelike region in three different ways. Firstly, we fit the individual timelike data with the  $\phi$ -meson parameters as free fit parameters, and the  $\omega(782)$  coupling fixed to  $c_\omega = c_\phi$  as predicted by  $SU(3)$ . Secondly, we fit the timelike data individually with  $c_\omega$  also a free parameter in addition to the  $\phi$  parameters. This gave an idea about the extent of  $\omega$  residue in the  $\phi$  region. Lastly, we fit the timelike data in combination with the spacelike data. Since the isovector part of the form factor dominates in the spacelike region, this gave an insight into the contribution of the isovector part to the full kaon electromagnetic form factor. The fits were done including the uncertainty band of the isovector part, which helped determine the relative uncertainty in the isovector calculation.

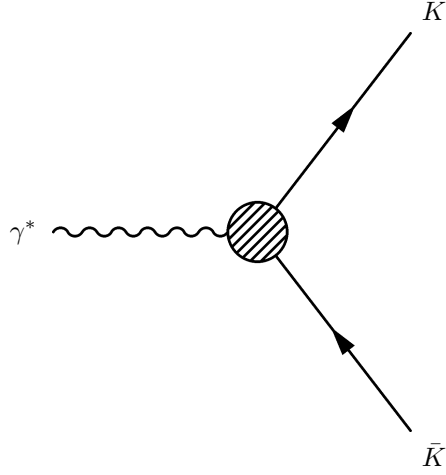


Figure 1.4: Diagram of kaon form factor.

The thesis is arranged as follows: In chapter 2, we introduce the mathematical and conceptual aspects of dispersion theory and proceed to calculate the pion vector form factor, which serves both as an example of dispersion relations, and is also an input to the kaon isovector form factor. The calculation of the isovector part of the kaon form factor using dispersion relations is presented in chapter 3. Chapter 4 is devoted to the calculation of the isoscalar part of kaon form factor. In chapter 5, we show the phenomenological fits to data in the timelike and spacelike regions and obtain the  $\phi$  parameters as well as the  $\omega$  coupling. Lastly, the results are summarised in chapter 6.



## Chapter 2

# Dispersion Relations

Dispersion relations connect the real part of a function to its imaginary part by an integral representation. In this chapter we discuss the unitarity of the  $\mathcal{S}$ -matrix and analytic relations of scattering amplitudes largely based on the concepts from [10]. We then discuss the pion form factor, which is an example for dispersion relations, and will subsequently be used in the calculation of the isovector part of the kaon form factor.

### 2.1 Unitarity

The full information about the scattering process is contained in the scattering matrix denoted by  $\mathcal{S}$ ,

$$\mathcal{S} = \mathbb{1} + i\mathcal{T}. \quad (2.1)$$

$\mathcal{T}$  denotes the transition amplitude or  $\mathcal{T}$ -matrix, which carries the non-trivial information about the interaction between the particles. The scattering amplitude  $\mathcal{M}$  is given by

$$(2\pi)^4 \delta^{(4)}(p_f - p_i) \mathcal{M}_{if} = \langle f | \mathcal{T} | i \rangle. \quad (2.2)$$

Here  $p_f$  and  $p_i$  are the 4-momenta of the final and initial states respectively.

Unitary relations follow from probability conservation, i.e., the total probability of a system evolving from initial state  $|i\rangle$  to final state  $|f\rangle$  must add up to 1:

$$1 = \sum_f |\langle f | \mathcal{S} | i \rangle|^2 = \sum_f \langle i | \mathcal{S}^\dagger | f \rangle \langle f | \mathcal{S} | i \rangle = \langle i | \mathcal{S}^\dagger \mathcal{S} | i \rangle. \quad (2.3)$$

This leads to the unitary relation for the  $\mathcal{S}$ -matrix,

$$\begin{aligned} \mathbb{1} &= \mathcal{S}^\dagger \mathcal{S} = \mathcal{S} \mathcal{S}^\dagger \\ &= (\mathbb{1} - i\mathcal{T}^\dagger)(\mathbb{1} + i\mathcal{T}) \\ &= \mathbb{1} - i(\mathcal{T}^\dagger - \mathcal{T}) + \mathcal{T}^\dagger \mathcal{T} \\ \implies i(\mathcal{T}^\dagger - \mathcal{T}) &= \mathcal{T}^\dagger \mathcal{T}. \end{aligned} \quad (2.4)$$

Inserting a complete set of intermediate states  $|n\rangle$ , we get for the transition amplitude

$$i \left( \langle f | \mathcal{T}^\dagger | i \rangle - \langle f | \mathcal{T} | i \rangle \right) = \sum_n \langle f | \mathcal{T}^\dagger | n \rangle \langle n | \mathcal{T} | i \rangle. \quad (2.5)$$

The scattering amplitude, by its definition, is then

$$\begin{aligned} i(2\pi)^4 \delta^{(4)}(p_f - p_i) (\mathcal{M}_{fi}^* - \mathcal{M}_{if}) &= \sum_n (2\pi)^4 \delta^{(4)}(p_f - p_n) \mathcal{M}_{fn}^* (2\pi)^4 \delta^{(4)}(p_n - p_i) \mathcal{M}_{in} \\ \implies i(\mathcal{M}_{fi}^* - \mathcal{M}_{if}) &= \sum_n d\Pi_n (2\pi)^4 \delta^{(4)}(p_f - p_n) \mathcal{M}_{fn}^* \mathcal{M}_{in}. \end{aligned} \quad (2.6)$$

The integration measure is the Lorentz invariant phase phase

$$d\Pi_n = \prod_{j \in n} \frac{d^4 k_j}{(2\pi)^4} (2\pi) \delta(k_j^2 - M_j^2) \Theta(k_j^0). \quad (2.7)$$

The Heaviside function  $\Theta$  takes only the positive energies, and  $j$  are the individual particles contributing to the intermediate state  $n$ .

## 2.2 Analyticity

Analyticity is the mathematical equivalent of causality, i.e., information cannot travel faster than the speed of light. To demonstrate this, we look at a simple square root function before continuing to a more generalised function with poles.

### Riemann Sheets

Consider the square function

$$g(x) = x^2. \quad (2.8)$$

The inverse function, or the square-root function is given by

$$f(x) = g^{-1}(x) = \pm\sqrt{x}. \quad (2.9)$$

It is a multi-valued function with two ambiguous solutions. The first solution  $f(x) = \sqrt{x}$ , which we consider to be the principal solution, has a branch cut from 0 to  $-\infty$  along the real axis as shown in fig. 2.1a. The point of singularity or the branch point is at  $x_0 = 0$ . The branch cut is described by the discontinuity

$$\text{disc} f(x) = \lim_{\epsilon \rightarrow 0} [f(x + i\epsilon) - f(x - i\epsilon)]. \quad (2.10)$$

Since the function  $g(x)$  is continuous, we introduce a second Riemann sheet for the unphysical solution as shown in fig. 2.1b. Then it is analytically continuous from the first to the second Riemann sheet.

For the purpose of physical applications, functions of the form  $\sqrt{x}$  are similar to  $\sqrt{s_{thr} - s}$ , and we can make a cut at  $s > s_{thr}$ . For a scattering amplitude, a pole on the real axis of the first (physical) Riemann sheet is a bound state. Any other poles are forbidden by analyticity. Poles on the second (unphysical) sheet are resonances. Intermediate states lead to discontinuities on the real axis. The location of a resonance pole is given by

$$s_{res} = \left( M_{res} - \frac{i}{2} \Gamma_{res} \right)^2, \quad (2.11)$$

where  $M_{res}$  and  $\Gamma_{res}$  are the mass and width of the resonance state. The branch point of the intermediate states, where the discontinuity starts is

$$s_{thr} = \left( \sum_i M_i \right)^2. \quad (2.12)$$

At this point, the intermediate particles of masses  $M_i$  can go on-shell and the discontinuity stretches to  $+\infty$ , hence called a right-hand cut. In every point, other than the singularities, the analytic continuation of the amplitude to the complex plane is holomorphic throughout.

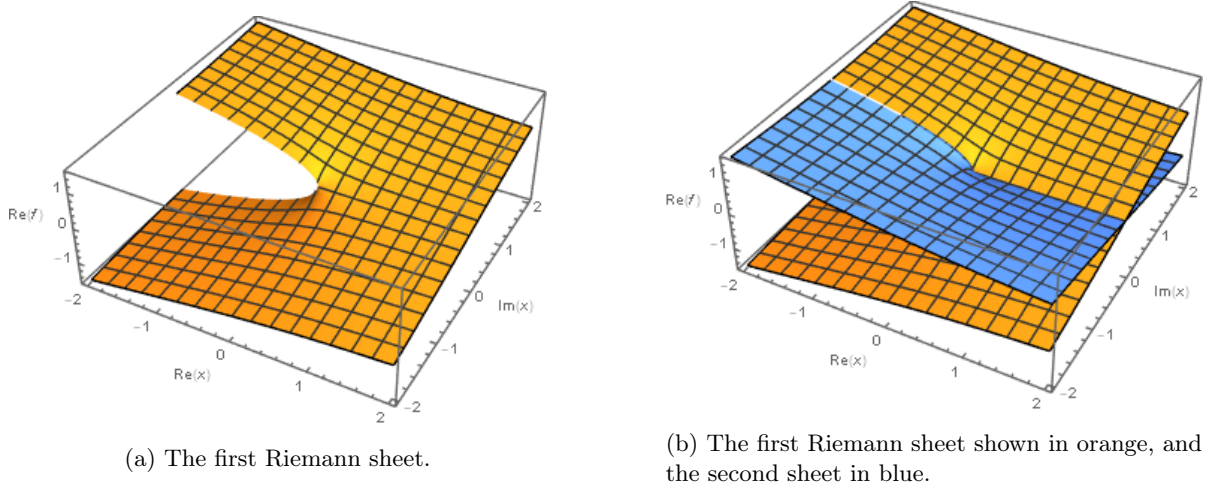


Figure 2.1: Riemann sheets for the square root function in eq. (2.9).

## Schwarz Reflection Principle

The Schwarz reflection principle states that if an analytic function has real values on segments of the real axis, it can be written as

$$f(x^*) = f^*(x). \quad (2.13)$$

The discontinuity of a function that satisfies the Schwarz reflection principle can be written in terms of its imaginary part,

$$\begin{aligned} \text{disc} f(x) &= \lim_{\epsilon \rightarrow 0} [f(x + i\epsilon) - f(x - i\epsilon)] \\ &= \lim_{\epsilon \rightarrow 0} [f(x + i\epsilon) - f^*(x + i\epsilon)] \\ &= 2i \text{Im} f(x). \end{aligned} \quad (2.14)$$

For the square root function in eq. (2.9), the real part remains the same in both sheets upon reflection along the real axis. However, the imaginary part flips sign. Hence, it satisfies the condition necessary for the Schwarz reflection principle.

## Cauchy's Integral Formula

Dispersion relations are derived starting from Cauchy's integral formula. A general holomorphic function  $f(x)$  with singularities can be computed using the relation

$$f(x) = \frac{1}{2\pi i} \oint_{\gamma} \frac{f(z)}{z - x} dz, \quad (2.15)$$

where  $\gamma$  is the integration contour as shown in fig. 2.2. The contour can be further divided into two separate contours  $\gamma_1$  (red line) and  $\gamma_2$  (blue line). The integration along contour  $\gamma_2$  vanishes for  $R \rightarrow \infty$  if  $f(x)|_{|x| \rightarrow \infty} \rightarrow 0$ .

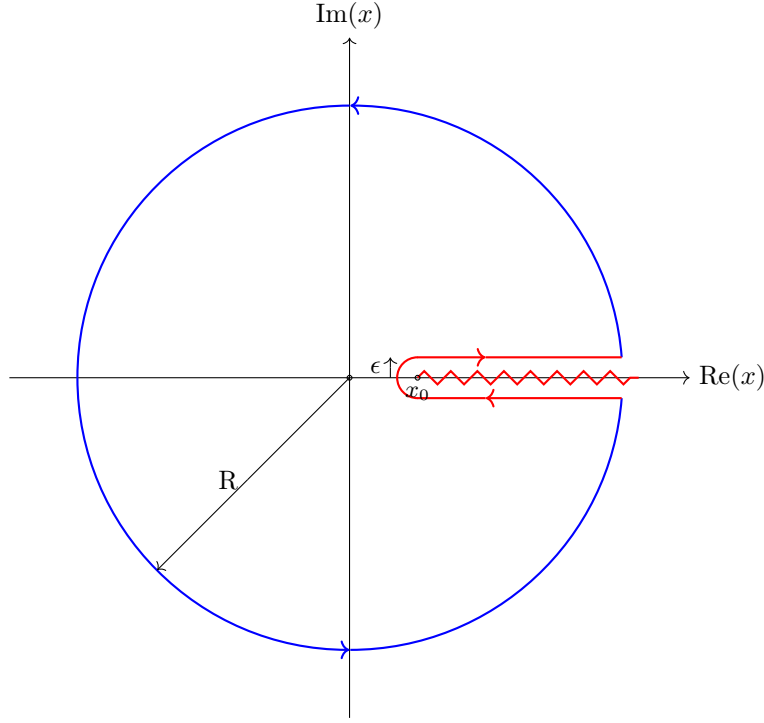


Figure 2.2: Integration contour of a function with a branch cut along the real axis. The red line corresponds to  $\gamma_1$  and the blue line is  $\gamma_2$ .

Then eq. (2.15) for  $\gamma_1$  is

$$\begin{aligned}
 f(x) &= \frac{1}{2\pi i} \oint_{\gamma} \frac{f(z)}{z-s} dz = \frac{1}{2\pi i} \left[ \int_{\gamma_1} \frac{f(z)}{z-s} dz + \int_{\gamma_2} \frac{f(z)}{z-s} dz \right] \\
 &= \lim_{\epsilon \rightarrow 0} \frac{1}{2\pi i} \left[ \int_{x_0}^{\infty} \frac{f(z+i\epsilon)}{z-x} dz + \int_{\infty}^{x_0} \frac{f(z-i\epsilon)}{z-x} dz \right] \\
 &= \frac{1}{2\pi i} \int_{x_0}^{\infty} \frac{\text{disc} f(z)}{z-x} dz \\
 &\stackrel{(2.14)}{=} \frac{1}{\pi} \int_{x_0}^{\infty} \frac{\text{Im} f(z)}{z-x} dz.
 \end{aligned} \tag{2.16}$$

This is the unsubtracted dispersion relation.

## Subtractions

Cauchy's integral formula can be directly used if the integrand is convergent, i.e., it approaches 0 faster than  $1/z$  for large  $z$ . If the integrand diverges, we need to do subtractions to be able to take  $R \rightarrow \infty$ . We rewrite

$$\frac{1}{z-x} = \frac{1}{z-y} + \frac{x-y}{(z-x)(z-y)}. \tag{2.17}$$

Thus, eq. (2.16) becomes

$$f(x) = \frac{1}{2\pi i} \oint_{\gamma} \frac{\text{disc} f(z)}{z-y} dz + \frac{1}{2\pi i} \oint_{\gamma} \frac{(x-y) \text{disc} f(z)}{(z-x)(z-y)} dz. \tag{2.18}$$

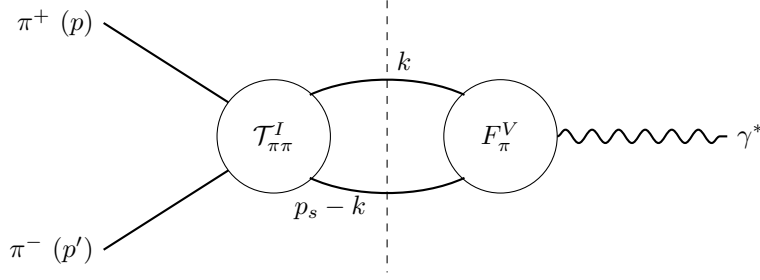


Figure 2.3: Diagrammatic representation of the discontinuity of pion vector form factor.

The first term is independent of  $x$  and is therefore a subtraction constant. The point  $y$  can be arbitrarily chosen below the branch point  $x_0$ . Thus,

$$\begin{aligned} f(x) &= f(y) + \frac{(x-y)}{2\pi i} \int_{x_0}^{\infty} \frac{\text{disc} f(z)}{(z-x)(z-y)} dz \\ &\stackrel{(2.14)}{=} f(y) + \frac{(x-y)}{\pi} \int_{x_0}^{\infty} \frac{\text{Im} f(z)}{(z-x)(z-y)} dz. \end{aligned} \quad (2.19)$$

This is a once-subtracted dispersion relation.

For a general function that grows asymptotically with  $\mathcal{O}(s^{N-1})$ , we can perform  $N$  subtractions.

$$f(x) = P_{N-1}(x) + \frac{\prod_{i=1}^N (x-y_i)}{2\pi i} \int_{x_0}^{\infty} \frac{\text{disc} f(z)}{\prod_{i=1}^N (z-y_i)(z-x)} dz, \quad (2.20)$$

where  $y_i$  are the subtraction points fulfilling  $y_i < x_0$ . There are  $N$  undetermined subtraction coefficients contained in the polynomials  $P$  of order  $N-1$ . The equation can be further simplified by setting all  $y_i = 0$ ,

$$\begin{aligned} f(x) &= P_{N-1}(x) + \frac{x^N}{2\pi i} \int_{x_0}^{\infty} \frac{\text{disc} f(z)}{z^N(z-x)} dz \\ &\stackrel{(2.14)}{=} P_{N-1}(x) + \frac{x^N}{\pi} \int_{x_0}^{\infty} \frac{\text{Im} f(z)}{z^N(z-x)} dz. \end{aligned} \quad (2.21)$$

## 2.3 Pion Vector Form Factor

In this section, the calculation of the pion vector form factor using the mathematical concepts discussed in the previous sections is shown. It will further be used in the calculation of the kaon isovector form factor discussed in chapter 3.

### 2.3.1 Watson's Final State Theorem

Consider the decay of a virtual photon to two charged pions as shown in fig. 2.3. The matrix element for the form factor is given by

$$\langle \pi^+(p) \pi^-(p') | J_\mu(0) | 0 \rangle = i(p-p')_\mu F_\pi^V(s), \quad (2.22)$$

where  $J_\mu$  is the electromagnetic current, and the Mandelstam variable  $s = (p+p')^2$ . We allow only  $\pi\pi$  intermediate states for elastic unitarity. The Cutkosky cutting rules [11] allow a cut through the diagram as shown in fig. 2.3. The intermediate pions are then put on-shell and the propagators are substituted with

$$\frac{1}{M_\pi^2 - k^2 - i\epsilon} \rightarrow -2\pi i \delta(k^2 - M_\pi^2). \quad (2.23)$$

The discontinuity in the pion form factor can then be calculated as

$$(p' - p)_\mu \text{disc} F_\pi^V(s) = \frac{i}{2} \int \frac{d^4 k}{(2\pi)^4} (2\pi) \delta(k^2 - M_\pi^2) (2\pi) \delta((p_s - k)^2 - M_\pi^2) \mathcal{T}_{\pi\pi}^{I*}(s, z_k) (p_s - 2k)_\mu F_\pi^V(s). \quad (2.24)$$

Here,  $\mathcal{T}_{\pi\pi}^I(s, z_k)$  is the  $\pi\pi$  scattering amplitude for isospin  $I$  which depends on the energy  $s$  and scattering angle  $z_k$  in the centre-of-mass frame, and  $p_s^2 = s = (p + p')^2$  is the centre-of-mass energy squared. Only the  $I = 1$  scattering phase shifts contribute due to Bose symmetry. Using the relation

$$\delta(f(x)) = \sum_{i=1}^n \frac{\delta(x - x_i)}{|f'(x_i)|}, \quad (2.25)$$

the delta functions are transformed as

$$\begin{aligned} \delta(k^2 - M_\pi^2) &= \frac{\delta(k_0 - \sqrt{k^2 + M_\pi^2})}{2\sqrt{k^2 + M_\pi^2}}, \\ \delta((p_s - k)^2 - M_\pi^2) &= \frac{\delta(k - \sqrt{s}\sigma_\pi(s)/2)}{2\sqrt{s}\sigma_\pi(s)}, \end{aligned} \quad (2.26)$$

where  $\sigma_\pi(s) = \sqrt{1 - 4M_\pi^2/s}$  is the phase-space factor. Then, substituting and implementing the delta functions, eq. (2.24) becomes

$$(p' - p)_\mu \text{disc} F_\pi^V(s) = \frac{i}{64\pi^2} \sigma_\pi(s) F_\pi^V(s) \int d\Omega_k \mathcal{T}_{\pi\pi}^1(s, z_k) (p_s - 2k)_\mu. \quad (2.27)$$

The right hand side of eq. (2.27) is now contracted with  $(p + p')_\mu$  and  $(p - p')_\mu$  in the centre-of-mass frame as shown in appendix A to find

$$\int d\Omega_z \mathcal{T}_{\pi\pi}^1(s, z_k) (p_s - 2k)_\mu = 2\pi (p - p')_\mu \int_{-1}^1 dz_k z_k \mathcal{T}_{\pi\pi}^1(s, z_k). \quad (2.28)$$

This integral can be solved further using a partial wave expansion of the form

$$\begin{aligned} \mathcal{T}_{\pi\pi}^1(s, z_k) &= 32\pi \sum_{l=0}^{\infty} (2l+1) t_l^1(s) P_l(z_k) \\ &= 64\pi t_1^1(s) z_k, \end{aligned} \quad (2.29)$$

where  $P_l$  are the Legendre polynomials and  $t_l^1$  is the  $\pi\pi$  scattering amplitude for a fixed angular momentum. Eq. (2.28) projects out only to  $P$ -waves, which has been used in the second line,  $l = 1 \implies P_1(z) = z$ . The partial wave in terms of the elastic phase shift is given by

$$t_1^1(s) = \frac{1}{\sigma_\pi} \sin \delta_1^1(s) e^{i\delta_1^1(s)}. \quad (2.30)$$

Inserting eqs. (2.28), (2.29) and (2.30) into eq. (2.27) and using eq. (2.14), we get for the imaginary part of the pion vector form factor

$$\text{Im} F_\pi^V(s) = F_\pi^V(s) \sin \delta(s) e^{-i\delta(s)} \Theta(s - 4M_\pi^2), \quad (2.31)$$

where  $\delta(s) = \delta_1^1(s)$ , and  $\Theta$  is the Heaviside step function.

Since  $\text{Im} F_\pi^V(s) \in \mathbb{R}$ , the right hand side of the equation must also be real. It follows that

$$F_\pi^V(s) = |F_\pi^V(s)| e^{i\delta(s)}, \quad (2.32)$$

which means that the phase of  $F_\pi^V(s)$  has to cancel out that of  $e^{i\delta(s)}$ , i.e., the phase of the form factor is equal to the phase of the final state elastic scattering amplitude. This is a direct consequence of Watson's final state theorem [12].

### 2.3.2 Omnès Solution

A solution to the form factor in eq. 2.32 is given by the Omnès function  $\Omega(s)$  [13]. Consider

$$\begin{aligned}\Omega(s + i\epsilon) &= |\Omega(s)|e^{i\delta(s)} \\ \Omega(s - i\epsilon) &= |\Omega(s)|e^{-i\delta(s)}.\end{aligned}\tag{2.33}$$

Then

$$\Omega(s - i\epsilon) = \Omega(s + i\epsilon)e^{-2i\delta(s)}.\tag{2.34}$$

Taking the logarithm of the above equation and using eq. (2.14), the discontinuity of the logarithm of the Omnès function is

$$\text{disc } \ln\Omega(s) = 2i\delta(s).\tag{2.35}$$

We assume that the Omnès function has no zeros. The above relation can be calculated using a dispersion relation. We use a once-subtracted dispersion relation, since the scattering phase shift  $\delta(s)$  is expected to become constant for  $s \rightarrow \infty$ :

$$\ln\Omega(s) = \ln\Omega(s_0) + \frac{s - s_0}{2\pi i} \int_{s_{th}}^{\infty} dz \frac{\text{disc } \ln\Omega(s)}{(z - s_0)(z - s)}.\tag{2.36}$$

Setting  $s_{th} = 4M_\pi^2$ , the physical threshold, and choosing  $s_0 = 0$  with the normalization  $\Omega(0) = 1$ , we finally obtain

$$\Omega(s) = \exp\left(\frac{s}{\pi} \int_{4M_\pi^2}^{\infty} dz \frac{\delta(z)}{z(z - s)}\right).\tag{2.37}$$

This is known as the Omnès solution. It is a general solution to the full pion vector form factor. The full solution is given by

$$F_\pi^V(s) = P(s)\Omega(s),\tag{2.38}$$

where  $P(s)$  is a real polynomial.

### 2.3.3 Computation of Pion Vector Form Factor

The input for scattering phase shift  $\delta(s)$  is the phase of the  $I = 1$   $\pi\pi \rightarrow K\bar{K}$   $P$ -wave taken from [14], shown in fig. 2.4. We use this phase to ensure that the phases of the partial wave and Omnès function cancel out in the computation of the isovector kaon form factor, making its imaginary part real by construction, as discussed in chapter 3. This phase shift is similar to the  $\pi\pi$  elastic phase shift below 1 GeV. It also includes the  $\pi$ - $\pi$  rescattering effects. Above a cutoff  $s_{cont} = (1.825\text{GeV})^2$ , we smoothly continue the phase to  $\pi$  using

$$\delta(s) = \pi - \frac{a}{b + s},\tag{2.39}$$

where  $a$  and  $b$  are chosen such that  $\delta(s)$  and its derivative are continuous at  $s_{cont}$ .

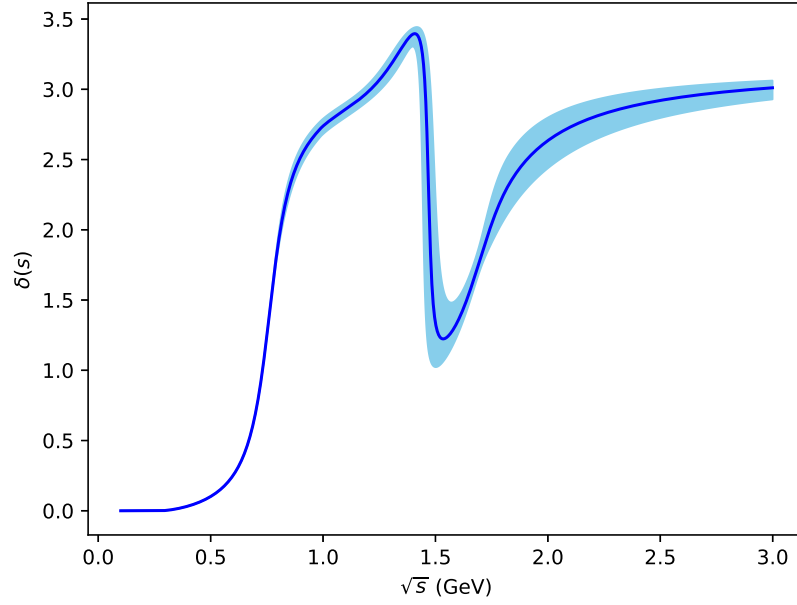
The polynomial  $P(s)$  is given by [15]

$$P(s) = 1 + \alpha s + \frac{\kappa s}{M_\omega^2 - s - i\Gamma_\omega M_\omega},\tag{2.40}$$

where the parameters  $\alpha$  and  $\kappa$  are obtained by fitting the Omnès function to BaBar pion form factor data [16] as shown in fig. 2.5. The fit results are given in table 2.1. The  $\omega$  term is included in the above equation because there is significant isospin-violating  $\rho - \omega$  mixing in the pion form factor. However, for the kaon form factor, we work in the isospin limit and therefore drop the  $\omega$ -resonance term and keep only the linear part of eq. (2.40). Furthermore, at high energies,  $s > (4\text{GeV})^2$ , we set the polynomial to a constant value. The full pion vector form factor, shown in fig. 2.6, is finally

$$F_\pi^V(s) = (1 + \alpha s) \cdot \exp\left(\frac{s}{\pi} \mathcal{P} \int_{4M_\pi^2}^{\infty} dz \frac{\delta(z)}{z(z - s - i\epsilon)} + i\delta(s)\right),\tag{2.41}$$

where  $\mathcal{P}$  represents the principal-value integral.

Figure 2.4:  $I = 1$   $P$ -wave scattering phase shift [14].

| Parameter                      | Upper bound           | Central value         | Lower bound           |
|--------------------------------|-----------------------|-----------------------|-----------------------|
| $\alpha$ ( $\text{GeV}^{-2}$ ) | $0.072 \pm 0.003$     | $0.169 \pm 0.001$     | $0.277 \pm 0.002$     |
| $\kappa$                       | $0.00241 \pm 0.00016$ | $0.00270 \pm 0.00007$ | $0.00296 \pm 0.00014$ |
| $M_\omega$ (MeV)               | $781.36 \pm 0.30$     | $781.67 \pm 0.66$     | $782.00 \pm 0.23$     |
| $\Gamma_\omega$ (MeV)          | $9.69 \pm 0.86$       | $10.08 \pm 0.35$      | $10.36 \pm 0.66$      |
| $\chi^2/\text{dof}$            | 11.051                | 1.615                 | 5.348                 |

Table 2.1: Fit results to BaBar data of pion form factor.



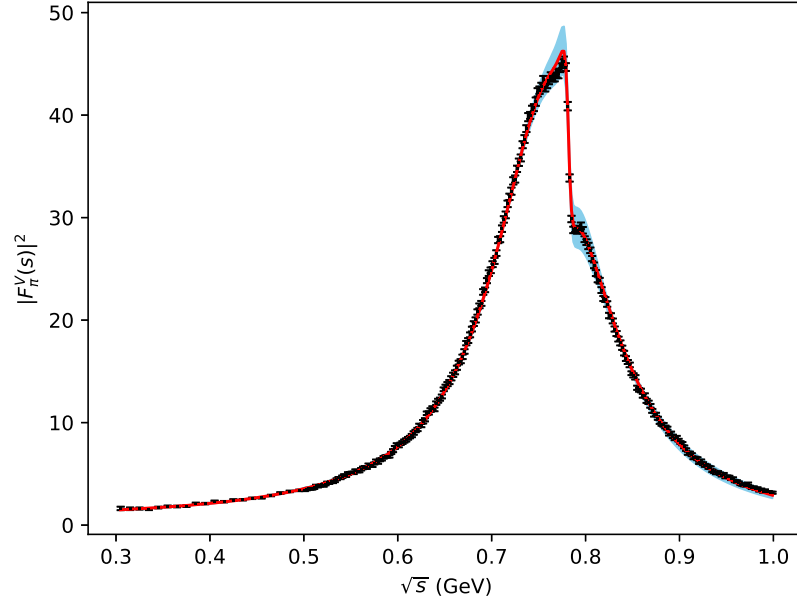


Figure 2.5: Fit to BaBar data [16].

The black lines are the data points, the red line is the fit using the central isovector value, and the blue band is the upper and lower isovector bounds.

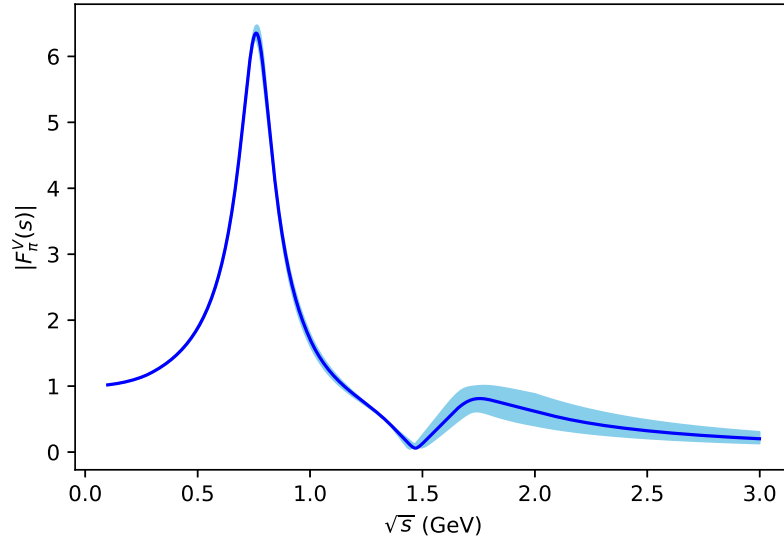


Figure 2.6: Pion vector form factor calculated using eq. (2.41).

## Chapter 3

# Isovector Part of the Kaon Form Factor

The isovector part of the kaon form factor is the dominant contribution in the spacelike ( $q^2 < 0$ ) region. The dominant isovector resonance  $\rho = \rho(770)$  is a broad resonance and cannot be approximated by the VMD model. Therefore we calculate its contribution dispersively, similar to the pion form factor. A dispersive calculation of this has been done previously in [8], where the authors calculated the isovector  $\rho$  contribution via a once-subtracted dispersion relation. This calculation is very old (1979) and there have been many improvements since then. The most significant improvement is the  $\pi\pi \rightarrow K\bar{K}$   $P$ -wave in [14] which is the main motivation behind this project. A lot of work has also been done pertaining the  $\tau$  leptons, and  $\tau$ -decays allows us to directly access the isovector kaon form factor. In the subsequent sections, we discuss the theoretical framework for calculating the isovector kaon form factor and compare our calculation to  $\tau$  decay data from [17].

### 3.1 Calculation of the Imaginary Part

Consider a photon of momentum  $p$  decaying into a kaon-antikaon pair via an intermediate two-pion state. The diagram for such a process is given in fig. 3.1. The first vertex is the pion vector form factor denoted by  $F_\pi^V$ , and the second is the  $\pi\pi \rightarrow K\bar{K}$  vertex denoted by  $G^I$ , where the  $I$  stands for the isospin. We work in the isospin limit and consider only one intermediate state. The contribution of the isovector part of the form factor to the total form factor is rather small, and this order of calculation is sufficient for the analysis we do. In particular, we chose the pion intermediate state because the pion form factor is relatively well understood to use as an input to the kaon form factor. Furthermore, there is not sufficient data for  $K\bar{K} \rightarrow K\bar{K}$  partial waves to use as an input here. In this section, we discuss the calculation of the imaginary part of the isovector kaon form factor using the relations derived in the previous chapter similar to the pion vector form factor.

The amplitude for photon decay to two kaons is given by

$$\mathcal{M}_{if} = \langle K(q_1)\bar{K}(q_2)|J_\mu(0)|0\rangle = e\epsilon^{\mu*}(q_1 - q_2)_\mu F_K^V(s), \quad (3.1)$$

where  $F_K^V(s)$  is the kaon isovector form factor. The diagram can be divided into two sections based on the Cutkosky cutting rules [11] similar to the pion vector form factor discussed in section 2.3. The left half is the pion vector form factor and the right half is the pions scattering to kaons. The amplitude for the pion form factor is

$$\mathcal{M}_{in} = \langle \pi^+(k_1)\pi^-(k_2)|J_\mu(0)|0\rangle = e\epsilon^{\mu*}(k_1 - k_2)_\mu F_\pi^V(s), \quad (3.2)$$

and the amplitude for the pions scattering to the pair of kaons is

$$\mathcal{M}_{fn} = G^I(s) = 16\pi\sqrt{2}\sum_l (2l+1)(q_\pi q_K)^l P_l(z) g_l^I(s). \quad (3.3)$$

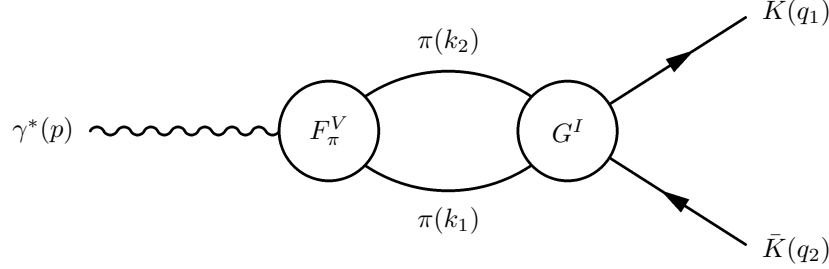


Figure 3.1: Diagram for kaon isovector form factor with a two-pion intermediate state.

We use the Bose symmetry to fix that only the  $I = 1$  waves contribute to the scattering. We work in the one-photon approximation here, and since electroweak currents are highly partial-wave selective, only the P-waves contribute to the scattering. The momenta  $q_\pi$  and  $q_K$ , given by  $q_{\pi/K} = \sqrt{s - 4M_{\pi/K}^2}/2$ , are the centre of mass momenta of the pseudoscalar particles.

Using the unitary properties of the matrix elements discussed in chapter 2, the three amplitudes can be equated via eq. (2.6). Writing the sum over all the intermediate states as a phase space integral, the amplitude for the kaon form factor is

$$\begin{aligned} \text{disc}\mathcal{M}_{if} &= i \sum_n (2\pi)^4 \delta^{(4)}(p_i - k_n) \mathcal{M}_{nf}^* \mathcal{M}_{in} \\ &= \frac{i}{4} \int \frac{d^4 k_1}{(2\pi)^4} \frac{d^4 k_2}{(2\pi)^4} (2\pi)^4 (2\pi) \delta(k_1^2 - M_\pi^2) (2\pi) \delta(k_2^2 - M_\pi^2) \mathcal{M}_{nf}^* \mathcal{M}_{in}, \end{aligned} \quad (3.4)$$

where the 4 in the denominator is due to symmetry of the process. Plugging in the relations for the different amplitudes from eqs. (3.1), (3.2) and (3.3), the discontinuity in the form factor is found to be

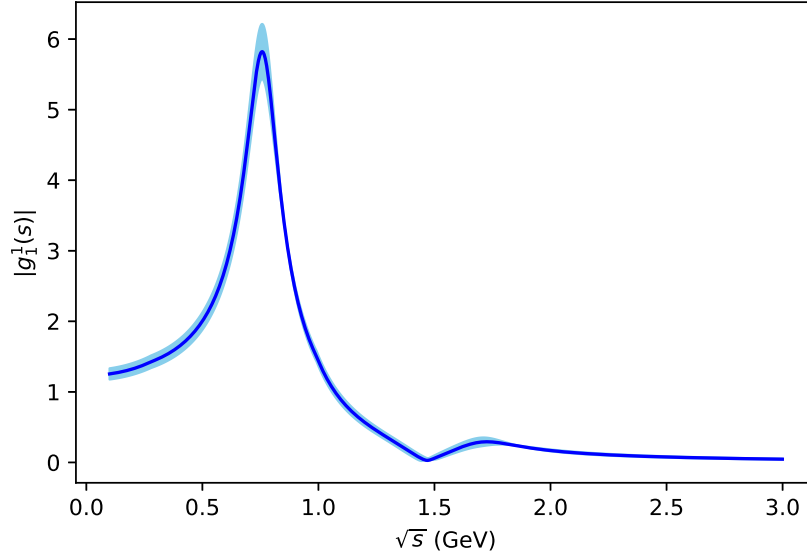
$$\begin{aligned} (q_1 - q_2)_\mu \text{disc}F_K(s) &= \frac{6i}{\sqrt{2}\pi} q_\pi q_K g_1^{1*}(s) F_\pi^V(s) \int d^4 k_1 d^4 k_2 \delta(k_1^2 - M_\pi^2) \delta(k_2^2 - M_\pi^2) (k_1 - k_2)_\mu z'' \\ &\stackrel{(A.4)}{=} \frac{3\sqrt{2}i}{16\pi} s \sigma_\pi^2 \sigma_K g_1^{1*}(s) F_\pi^V(s) \int d\Omega (2k_1 - p)_\mu z'' \\ &\stackrel{(A.9)}{=} \frac{i}{2\sqrt{2}} s \sigma_\pi^3 g_1^{1*}(s) F_\pi^V(s) (q_1 - q_2)_\mu, \end{aligned} \quad (3.5)$$

where the relation  $q_{\pi/K} = \sigma_{\pi/K} \sqrt{s}/2$  has been used in the second line. Using eq. (2.14), the imaginary part of the kaon form factor is then found to be [8]

$$\text{Im}F_K(s) = \frac{s}{4\sqrt{2}} \sigma_\pi^3 g_1^{1*}(s) F_\pi^V(s). \quad (3.6)$$

The form of the partial wave  $g_1^1(s)$ , shown in fig. 3.2, is taken from [14] up to a threshold of  $s_{cont} = (1.825\text{GeV})^2$ . Beyond that, we used the modified function

$$g_1^1(s) = \frac{p}{s - q}, \quad (3.7)$$

Figure 3.2: Partial wave  $g_1^1(s)$ .

to use less computational power at arbitrarily high energies. The constants  $p$  and  $q$  were determined such that both  $g_1^1(s)$  and its derivative are continuous at  $s_{cont}$ . The pion vector form factor  $F_\pi^V(s)$  was determined using the Omnès solution as discussed in chapter 2. We use the constrained fit to data (CFD) parameters for the partial wave and the pion vector form factor in our model. The CFD parameters were determined by constraining the fit to the partial wave data by constraints such as hyperbolic dispersion relations and fixed- $t$  dispersion relations among others. Since the phase for the Omnès function is the phase of the partial wave  $g_1^1(s)$ , the phases cancel out and  $\text{Im}F_K(s)$  is real by construction.

### 3.2 Computing Full Isovector Kaon Form Factor

The real part of the isovector form factor can be calculated from the imaginary part using dispersion relations as discussed in the case of the Omnès function in chapter 2.

Using eq. (2.16), we write the real part of the isovector form factor as an unsubtracted dispersion relation

$$\text{Re}F_K(s) = \frac{1}{\pi} \int_{4M_\pi^2}^{\infty} \frac{\text{Im}F_K(z)}{z-s} dz. \quad (3.8)$$

Using the Sokhotski-Plemelj theorem, the full form factor is

$$F_K(s) = \frac{1}{\pi} \mathcal{P} \int_{4M_\pi^2}^{\infty} \frac{\text{Im}F_K(z)}{z-s} dz + \text{Im}F_K(s). \quad (3.9)$$

The above form factor gives only the contribution of the  $\rho$ -resonance. The higher  $\rho' = \rho(1450)$  and  $\rho'' = \rho(1690)$  states are partially included in  $g_1^1(s)$ , but they are suppressed during the calculation of the dispersion integral, and the normalisation sum rule at  $s = 0$  of the dispersion relation does not output the expected  $1/2$ . There are also some inelastic effects not included in the calculation so far but are present in the process. We account for these effects by including the  $\rho'$  resonance using the

| Parameter         | Upper bound | Central value | Lower bound |
|-------------------|-------------|---------------|-------------|
| $F_K^\rho(0)$     | 0.54877     | 0.53738       | 0.53140     |
| $\lambda_{\rho'}$ | -0.04877    | -0.03738      | -0.03140    |

Table 3.1: Value of  $\rho$  and  $\rho'$  couplings.

vector meson dominance model to approximate its contribution by a Breit-Wigner function. It would not be appropriate to do a full dispersive calculation for the  $\rho'$  because it couples to  $4\pi$  and  $\pi\omega$  states in addition to the  $\pi\pi$  state that we are concerned with. The contribution of the  $\rho'$  is also very small and an approximation as a Breit-Wigner function is sufficient. The function is of the form

$$F_K^{\rho'}(s) = \frac{\lambda_{\rho'} M_{\rho'}^2}{M_{\rho'}^2 - s - iM_{\rho'} \Gamma_{\rho'}(s)}, \quad (3.10)$$

where  $\Gamma_{\rho'}(s)$  is the  $s$ -dependent width of  $\rho'$  [14],

$$\Gamma_{\rho'}(s) = \frac{\Gamma_{\rho'} \sqrt{s} (2G_\pi(s) + G_K(s))}{2M_{\rho'} G_\pi(M_{\rho'}^2)}, \quad (3.11)$$

where  $\Gamma_{\rho'}$  is the full width of  $\rho'$ . The function  $G_P(s)$ , where  $P$  denotes the pseudoscalars  $\pi/K$ , is given by

$$G_P(s) = \sqrt{s} \left( \frac{2q_P(s) \Theta(s - 4M_P^2)}{\sqrt{s}} \right)^3. \quad (3.12)$$

$\lambda_{\rho'}$  in eq. (3.10) is the  $\rho'$  coupling determined by the normalization condition at  $s = 0$ ,

$$\begin{aligned} F_K^V(0) &= \frac{1}{2} = F_K^\rho(0) + F_K^{\rho'}(0) \\ &= \frac{1}{\pi} \int_{4M_\pi^2}^{\infty} \frac{\text{Im} F_K(z)}{z} dz + \lambda_{\rho'}. \end{aligned} \quad (3.13)$$

The value of the coupling  $\lambda_{\rho'}$  is given in table 3.10. It is noted that the  $\rho'$  coupling is very small. Its relative sized is similar compared to what was seen for the pion form factor [18] by fit to  $\tau \rightarrow \pi^- \pi^0 \nu_\tau$  data from Belle [19].

The full isovector kaon form factor is finally

$$F_K^V(s) = \left[ \frac{1}{\pi} \mathcal{P} \int_{4M_\pi^2}^{\infty} \frac{\text{Im} F_K^\rho(z)}{z - s} dz + \text{Im} F_K^\rho(s) \right] + \frac{\lambda_{\rho'} M_{\rho'}^2}{M_{\rho'}^2 - s - iM_{\rho'} \Gamma_{\rho'}(s)}. \quad (3.14)$$

The graphical representation is shown in fig. 3.3.

The average difference throughout the plot for the lower and upper error bounds in comparison with the central value is 7.7% and 6.9%, respectively. At the  $\rho$  peak, the difference is 7.9% and 8.3%, respectively. Therefore our isovector calculation works within a 10% confidence level.

### 3.3 Comparison with BaBar Data

The isovector part of the form factor can be separately analysed from  $\tau^- \rightarrow K^- K_S \nu_\tau$  decay as done in [17]. Such a decay is purely isovector because it is a charged current process involving the  $W^\pm$  boson

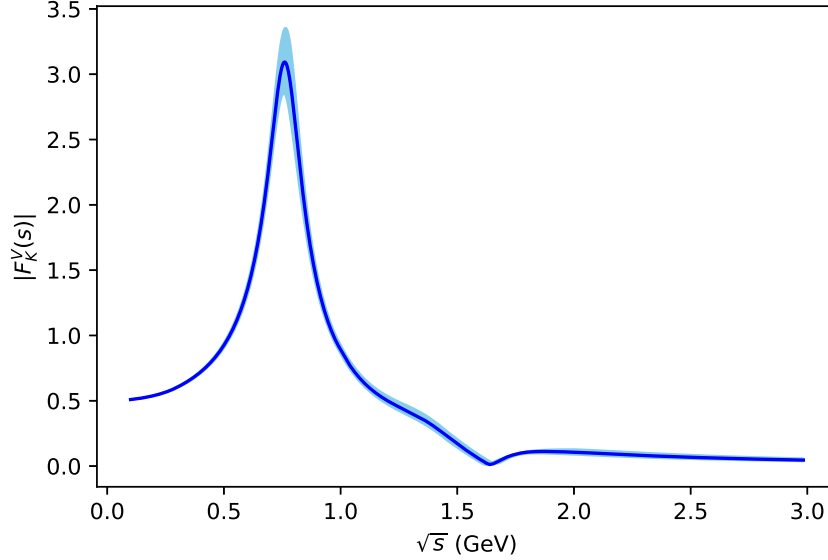


Figure 3.3: Isovector part of kaon form factor.

which has isospin  $I = \pm 1$ . The vector spectral function  $v_1$  in the decay is related to the isovector form factor because of the conserved vector current [17] via

$$v_1 = \frac{1}{4\pi} \frac{\sigma_K^3}{3} |F_K^V(s)|^2. \quad (3.15)$$

The spectral function for the  $\tau$  decay was obtained experimentally from BaBar [20]. We compare our isovector results to the BaBar kaon isovector form factor data as shown in fig. 3.4. The red line corresponds to the computation of the isovector form factor using the CFD values in the partial wave as discussed before. The blue region shows the uncertainty band of the isovector form factor. The green line corresponds to the form factor computation using the unconstrained fit to data (UFD) values for the partial wave  $g_1^1(s)$  and Omnès function from [14]. The UFD values were determined by individual fits to various  $\pi\pi \rightarrow K\bar{K}$  and  $\pi K \rightarrow \pi K$  data without any particular constraints. The CFD results are more theoretically reliable because the error in estimation of systematic uncertainties and partially conflicting datasets is reduced significantly in fits with constraints.

Clearly, in fig. 3.4, there is a significant shift in our values using CFD results as compared to the data. The UFD parameters seem to fit much better. However, since the CFD parameters are much more reliable, we continue our analysis with the same. Moreover, since we concentrate more on the  $\rho$ -region of the isovector part for the phenomenological analysis, this shift can be ignored.

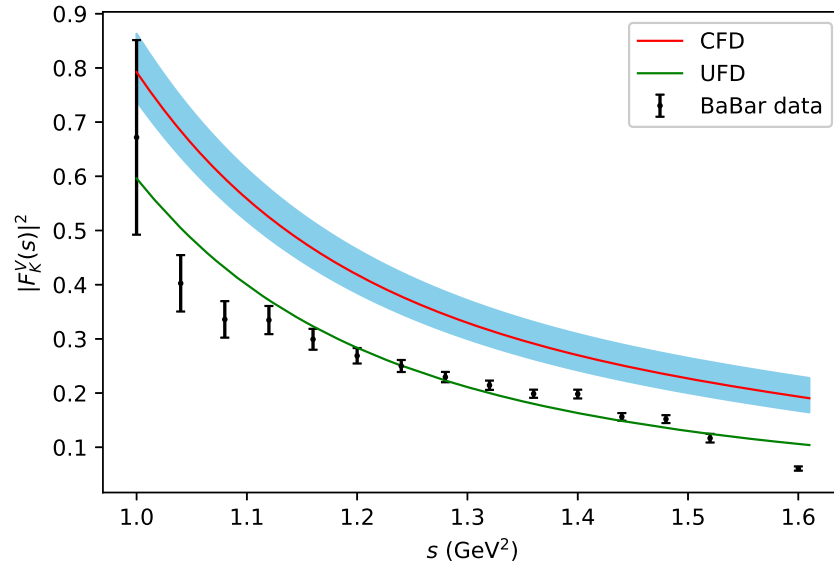


Figure 3.4: Comparison of our isovector results with BaBar data from  $\tau \rightarrow K^- K_S \nu_\tau$  decay. The red line with blue band is the isovector kaon form factor computed using CFD values and the green line is the form factor computed using UFD values. The black lines are the BaBar data.

## Chapter 4

# Isoscalar Part of the Kaon Form Factor

In this chapter, we discuss the isoscalar part of the kaon form factor derived from the relevant Lagrangians from [9]. There is a significant  $\omega \rightarrow 3\pi$  decay and  $K\bar{K}$  intermediate state in the isoscalar channel. Doing a full dispersive calculation is not possible because of lack of reliable input for the phase of this. Furthermore, the isoscalar resonances  $\omega = \omega(782)$  and  $\phi = \phi(1020)$  have relatively narrow widths as opposed to their masses:

$$\begin{aligned} M_\omega &= 782.66 \pm 0.13 \text{ MeV} & \Gamma_\omega &= 8.68 \pm 0.13 \text{ MeV}, \\ M_\phi &= 1019.461 \pm 0.016 \text{ MeV} & \Gamma_\phi &= 4.249 \pm 0.013 \text{ MeV}, \end{aligned}$$

in contrast to the isovector  $\rho$ :

$$M_\rho = 775.26 \pm 0.23 \text{ MeV} \quad \Gamma_\rho = 147.4 \pm 0.8 \text{ MeV}.$$

Hence, the  $\omega$  and  $\phi$  contributions can be approximated by Breit-Wigner resonances based on a  $SU(3)$ -symmetric Lagrangian instead of doing a full dispersive calculation.

The tree level diagram for photon decay to kaons via the isoscalar channel is shown in fig. 4.1. The interaction Lagrangian for this process is given by [9]:

$$\begin{aligned} \mathcal{L}_{\text{int}} &= \mathcal{L}_{\gamma V} + \mathcal{L}_{V\Phi\Phi} \\ &= \frac{-e}{2g_V} F^{\mu\nu} \text{tr}(QG_{\mu\nu}) + \frac{ig}{4} \text{tr}(V^\mu [\partial_\mu \Phi, \Phi]). \end{aligned} \quad (4.1)$$

$\Phi$  represents the pseudoscalar particles ( $\pi, K$ ) and  $V_\mu$  represents the neutral vector mesons ( $\rho, \omega, \phi$ ). The matrix form of the pseudoscalar fields is

$$\Phi = \sqrt{2} \begin{pmatrix} \frac{\pi^0}{\sqrt{2}} & \pi^+ & K^+ \\ \pi^- & \frac{-\pi^0}{\sqrt{2}} & K^0 \\ K^- & \frac{\sqrt{2}}{2} & 0 \end{pmatrix}, \quad (4.2)$$

and that of the flavour-neutral vector resonances is

$$V_\mu = \begin{pmatrix} \rho + \omega & 0 & 0 \\ 0 & -\rho + \omega & 0 \\ 0 & 0 & \sqrt{2}\phi \end{pmatrix}_\mu. \quad (4.3)$$

The diagram can be divided into two parts; electron-positron annihilation to a vector meson via a photon propagator and the vector meson decaying to a pair of kaons. The couplings  $g$  and  $g_\gamma$  are fixed from these individual processes which shall be further discussed.



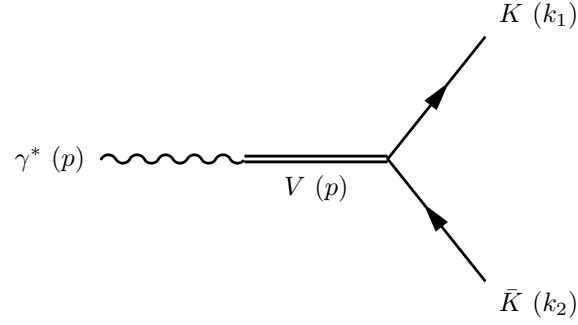
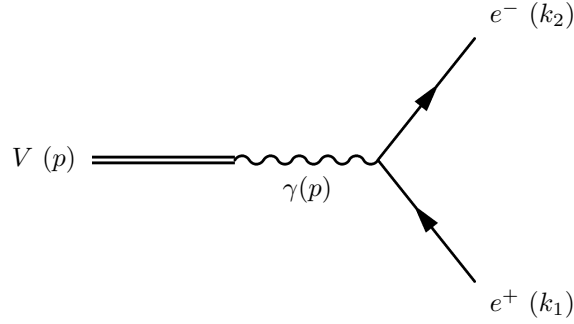


Figure 4.1: Diagram for photon decaying to kaons in the isoscalar channel.

Figure 4.2: Diagram for the  $\gamma V$  vertex.

## 4.1 $\gamma V$ Vertex

The interaction Lagrangian for the process  $V \rightarrow \gamma^* \rightarrow e^+ e^-$  as shown in fig. 4.2 is

$$\mathcal{L}_{\gamma V} = \frac{-e}{2g_V} F^{\mu\nu} \text{tr}(Q G_{\mu\nu}), \quad (4.4)$$

where  $G_{\mu\nu} = \partial_\mu V_\nu - \partial_\nu V_\mu$  and  $F^{\mu\nu} = \partial^\mu A^\nu - \partial^\nu A^\mu$  are the field strength tensor for the vector and photon fields respectively, and  $Q = \text{diag}[2/3, -1/3, -1/3]$  is the quark charge matrix. Using these definitions, we get

$$\begin{aligned} \mathcal{L}_{\gamma V} &= \frac{-e}{2g_V} F^{\mu\nu} \text{tr} \begin{pmatrix} \frac{2}{3}[\partial_\mu \omega_\nu - \partial_\nu \omega_\mu] & 0 & 0 \\ 0 & -\frac{1}{3}[\partial_\mu \omega_\nu - \partial_\nu \omega_\mu] & 0 \\ 0 & 0 & -\frac{\sqrt{2}}{3}[\partial_\mu \phi_\nu - \partial_\nu \phi_\mu] \end{pmatrix} \\ &= \frac{-e}{2g_V} F^{\mu\nu} \left( \frac{1}{3}[\partial_\mu \omega_\nu - \partial_\nu \omega_\mu] - \frac{\sqrt{2}}{3}[\partial_\mu \phi_\nu - \partial_\nu \phi_\mu] \right). \end{aligned} \quad (4.5)$$

The matrix element for the direct conversion of a photon into a vector meson is given by [9]

$$\langle V(p) | \gamma(p) \rangle = -\frac{e}{g_V} p^2 \epsilon(p) \cdot \bar{\epsilon}(p). \quad (4.6)$$

The matrix element of the full process is then

$$\begin{aligned} i\mathcal{M} &= \bar{\epsilon}_\nu^*(p) \left( \frac{-e}{g_V} p^2 \right) \left( \frac{-ig^{\nu\mu}}{p^2} \right) \bar{u}(k_2) (-ie\gamma_\mu) v(k_1) \\ &= \frac{e^2}{g_V} \bar{\epsilon}_\nu^*(p) \bar{u}(k_2) \gamma^\nu v(k_1), \end{aligned} \quad (4.7)$$

where  $\bar{\epsilon}$  represents the polarization vector of the vector particle, and  $u$  and  $v$  are the fermionic spinors.

Averaging over the initial and summing over the final spins, the squared amplitude is

$$|\overline{\mathcal{M}}|^2 = \frac{1}{3} \frac{e^4}{g_V^2} \sum_{\text{spins}} \bar{\epsilon}_\nu^*(p) \bar{\epsilon}_\mu(p) \bar{u}(k_2) \gamma^\nu v(k_1) \bar{v}(k_1) \gamma^\mu u(k_2). \quad (4.8)$$

The spins sums for the polarization vector and fermions are given by

$$\begin{aligned} \sum_i \bar{\epsilon}_\nu^*(p) \bar{\epsilon}_\mu(p) &= -g_{\nu\mu} + \frac{p_\nu p_\mu}{p^2}, \\ \sum \bar{u}(k_2) \gamma^\nu v(k_1) \bar{v}(k_1) \gamma^\mu u(k_2) &= 4(k_1^\nu k_2^\mu - \eta^{\nu\mu} k_1 \cdot k_2 + k_1^\mu k_2^\nu). \end{aligned} \quad (4.9)$$

Therefore, multiplying the expressions, the squared amplitude is found to be

$$|\overline{\mathcal{M}}|^2 = \frac{4e^4}{3g_V^2} \left( (k_1 \cdot k_2) - \frac{1}{p^2} [2(k_1 \cdot p)(k_2 \cdot p) - p^2(k_1 \cdot k_2)] \right). \quad (4.10)$$

Using the conservation of four-momentum,  $p = k_1 + k_2$ , the products of the momenta can be obtained as follows

$$\begin{aligned} (k_1 \cdot p)(k_2 \cdot p) &= (k_1 \cdot (k_1 + k_2))(k_2 \cdot (k_1 + k_2)) \\ &= (k_1 \cdot k_2)^2 \\ &= \left( \frac{1}{2} [k_1^2 + k_2^2 - (k_1 + k_2)^2] \right)^2 \\ &= \frac{1}{4} p^4 = \frac{M_V^4}{4}, \end{aligned} \quad (4.11)$$

where  $k_1^2 = k_2^2 = M_e^2 \approx 0$  was used in the fourth line. Finally, the amplitude of the process is

$$|\overline{\mathcal{M}}|^2 = \frac{2e^4}{3g_V^2} M_V^2. \quad (4.12)$$

The partial width for a two-particle decay process is calculated with the relation [21]

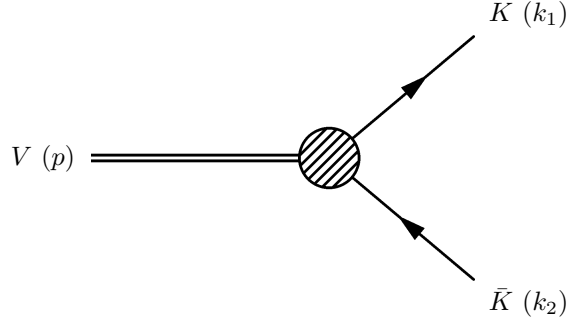
$$\frac{d\Gamma}{d\Omega} = \frac{1}{32\pi^2} |\mathcal{M}|^2 \frac{|\mathbf{p}_{cms}|}{M_V^2} d\Omega. \quad (4.13)$$

$\mathbf{p}_{cms}$  is the rest frame momentum of the outgoing particles, which is  $|\mathbf{p}_{cms}| = M_V$  for this process. Plugging in the quantities, we obtain the decay width

$$\Gamma_V = \frac{e^4 M_V}{12\pi g_V^2} = \frac{4\pi\alpha^2 M_V}{3g_V^2}, \quad (4.14)$$

where  $\alpha = e^2/4\pi$  is the fine structure constant. Using the PDG average for the various quantities [21], the coupling for individual vector mesons are calculated. The couplings are given in table 4.1.  $SU(3)$  and eq. (4.5) predict the ratio of the couplings  $g_\omega : g_\phi = 3 : -3/\sqrt{2}$ . Then a universal coupling  $g_\gamma$  for such a process can be calculated using the relation  $g_\omega = -\sqrt{2}g_\phi = 3g_\gamma$ , which would help simplify the calculation for the full diagram. The universal coupling calculated using the  $\omega$  parameters is given in table 4.1. The universal coupling calculated using the  $\phi$  mass and width deviates by about 12% compared to  $\omega$ .

| Process                     | Partial Width (keV) | Coupling $g_V$    | $g_\gamma$      |
|-----------------------------|---------------------|-------------------|-----------------|
| $\omega \rightarrow e^+e^-$ | $0.64 \pm 0.02$     | $16.50 \pm 0.24$  | $5.56 \pm 0.08$ |
| $\phi \rightarrow e^+e^-$   | $1.26 \pm 0.02$     | $-13.42 \pm 0.08$ |                 |

Table 4.1: Couplings for  $e^+e^- \rightarrow V$ .Figure 4.3: Diagram for  $V \rightarrow K\bar{K}$ .

## 4.2 $V\Phi\Phi$ Vertex

In this section, the second part of fig. 4.1 is considered, i.e., vector meson decaying to a kaon-antikaon pair, shown in fig. 4.3. The derivation is similar to the work presented in [22]. The interaction Lagrangian is

$$\mathcal{L}_{V\Phi\Phi} = \frac{ig}{4} \text{tr}(V^\mu [\partial_\mu \Phi, \Phi]). \quad (4.15)$$

The pion entries in  $\Phi$ , and the isovector  $\rho$  in  $V_\mu$  are neglected. The trace is then

$$\begin{aligned} \text{tr}(V^\mu [\partial_\mu \Phi, \Phi]) &= 2 \begin{pmatrix} \omega & 0 & 0 \\ 0 & \omega & 0 \\ 0 & 0 & \sqrt{2}\phi \end{pmatrix}^\mu \left[ \partial_\mu \begin{pmatrix} 0 & 0 & K^+ \\ 0 & 0 & K^0 \\ K^- & \bar{K}^0 & 0 \end{pmatrix}, \begin{pmatrix} 0 & 0 & K^+ \\ 0 & 0 & K^0 \\ K^- & \bar{K}^0 & 0 \end{pmatrix} \right] \\ &= 2\omega^\mu (\partial_\mu K^+ K^- - K^+ \partial_\mu K^-) + 2\sqrt{2}\phi^\mu (\partial_\mu K^- K^+ - K^- \partial_\mu K^+) \\ &\quad + 2\omega^\mu (\partial_\mu K^0 \bar{K}^0 - K^0 \partial_\mu \bar{K}^0) + 2\sqrt{2}\phi^\mu (\partial_\mu \bar{K}^0 K^0 - \bar{K}^0 \partial_\mu K^0). \end{aligned} \quad (4.16)$$

Hence, the Lagrangian is

$$\begin{aligned} \mathcal{L}_{V\Phi\Phi} &= \frac{ig}{2} (\omega - \sqrt{2}\phi)^\mu (\partial_\mu K^+ K^- - K^+ \partial_\mu K^-) \\ &\quad + \frac{ig}{2} (\omega - \sqrt{2}\phi)^\mu (\partial_\mu K^0 \bar{K}^0 - K^0 \partial_\mu \bar{K}^0). \end{aligned} \quad (4.17)$$

The matrix element for the above Lagrangian is given by

$$i\mathcal{M} = \frac{g}{\sqrt{2}} \bar{\epsilon}_\mu^*(p) i(k_2^\mu - k_1^\mu). \quad (4.18)$$

The squared amplitude is

$$\begin{aligned}
|\overline{\mathcal{M}}|^2 &= \frac{g^2}{6} \sum_{\text{spins}} \epsilon_\mu^*(p) \bar{\epsilon}_\nu(p) (k_2^\mu - k_1^\mu) (k_2^\nu - k_1^\nu) \\
&\stackrel{(4.9)}{=} \frac{g^2}{6} \left[ -g_{\mu\nu} (k_2^\mu - k_1^\mu) (k_2^\nu - k_1^\nu) + \frac{p_\mu p_\nu}{q^2} (k_2^\mu - k_1^\mu) (k_2^\nu - k_1^\nu) \right] \\
&= \frac{g^2}{6} \left[ (k_2 - k_1)^2 + \frac{1}{p^2} (p \cdot (k_2 - k_1))^2 \right].
\end{aligned} \tag{4.19}$$

Using the conservation of momentum  $p = k_1 + k_2$  and the relations  $k_1^2 = k_2^2 = M_K^2$ ,  $p^2 = M_V^2$ , the squared amplitude is finally

$$|\overline{\mathcal{M}}|^2 = \frac{g^2}{6} (M_V^2 - 4M_K^2). \tag{4.20}$$

Using the two-particle decay width from eq. (4.13), the decay width for this process is found to be

$$\begin{aligned}
\Gamma_V &= \frac{1}{32\pi^2} 4\pi \frac{g^2}{6} (M_V^2 - 4M_K^2) \frac{\sqrt{M_V^2 - 4M_K^2}}{2M_V^2} \\
&= \frac{g^2}{96\pi} M_V \left( 1 - \frac{4M_K^2}{M_V^2} \right)^{3/2}.
\end{aligned} \tag{4.21}$$

The coupling can now be fixed from the experimental values of the widths and masses from [21]. The coupling calculated using  $\phi$  mass and width, corresponding to charged kaons is

$$g = 6.33 \pm 0.03. \tag{4.22}$$

The decay  $\omega \rightarrow K\bar{K}$  is kinematically forbidden since  $M_\omega < 2M_K$ . Therefore we fix the coupling  $g$  from  $\phi \rightarrow K\bar{K}$  decay alone and rely on the  $SU(3)$  prediction that the coupling is universal. The value of coupling calculated from  $\phi \rightarrow K\bar{K}$  deviates from the coupling calculated via  $\rho \rightarrow 2\pi$  by only about 6%, as shown in [23]. Therefore a universal coupling  $g$  for all three vector meson vertices is expected to work in the 10% level. We also phenomenologically test the universality of this coupling, discussed in chapter 5.

### 4.3 Full Diagram

Using the couplings from the two vertices, we can now calculate the tree level diagram in fig. 4.1.

The propagator of a massive stable vector particle is given by

$$-\frac{i}{p^2 - M_V^2} \left( g_{\kappa\lambda} - \frac{p_\kappa p_\lambda}{p^2} \right). \tag{4.23}$$

The amplitude for  $\gamma^* \rightarrow K\bar{K}$  is

$$\begin{aligned}
i\mathcal{M} &= \epsilon_\mu^*(p) p_\nu \left( -\frac{ie}{2g_V} 2p^\nu \right) \left[ -\frac{i}{p^2 - M_V^2} \left( g_{\kappa\lambda} - \frac{p_\kappa p_\lambda}{p^2} \right) \right] \left( \frac{ig_{cV}}{\sqrt{2}} (k_1^\lambda - k_2^\lambda) \right) \\
&= -\frac{ieg_{cV}}{\sqrt{2}g_V} \frac{1}{p^2 - M_V^2} \epsilon_\mu^*(p) \left[ p_\nu p^\nu g_{\kappa\lambda} (k_1 - k_2)^\lambda - p_\nu p^\nu \frac{p_\kappa p_\lambda}{p^2} (k_1 - k_2)^\lambda \right] \\
&\stackrel{p=k_1+k_2}{=} -\frac{ieg_{cV}}{\sqrt{2}g_V} \frac{1}{p^2 - M_V^2} \epsilon_\mu^*(p) \left[ p^2 (k_1 - k_2)_\kappa - p_\kappa (k_1 + k_2) \cdot (k_1 - k_2) \right] \\
&\stackrel{k_1^2=k_2^2=M_K^2}{=} -\frac{ieg_{cV}}{\sqrt{2}g_V} \frac{1}{p^2 - M_V^2} \epsilon_\mu^*(p) p^2 (k_1 - k_2)_\kappa.
\end{aligned} \tag{4.24}$$

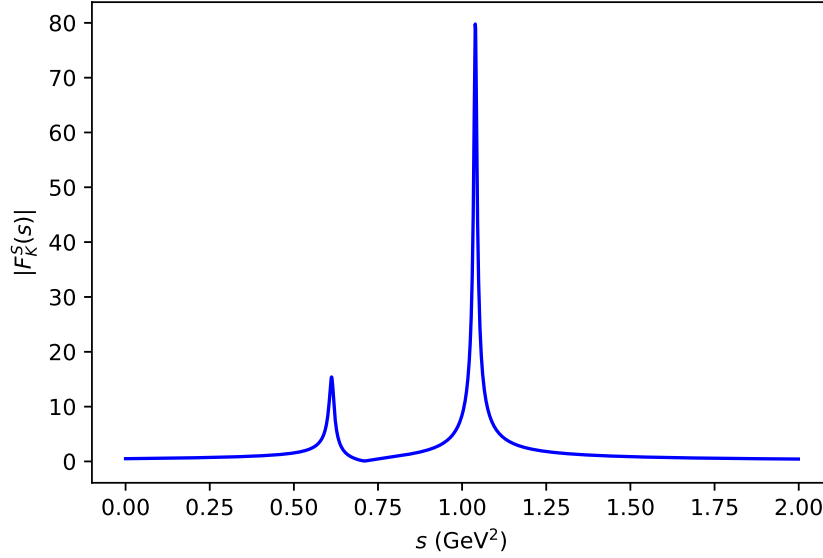


Figure 4.4: Isoscalar kaon form factor.

We have used the conservation of four-momentum and relativistic relations. Here  $c_V$  is the  $SU(3)$  factor for the massive vector particles

$$c_V = \begin{cases} -\frac{1}{\sqrt{2}}, & V = \omega \\ +1, & V = \phi \end{cases}. \quad (4.25)$$

The general form of matrix element for kaon form factor is given by

$$\langle K(k_1) \bar{K}(k_2) | J_\kappa(0) | 0 \rangle = i(k_1 - k_2)_\kappa F_K(s). \quad (4.26)$$

Therefore by comparison of eqs. (4.24) and (4.26), and using  $p^2 = M_V^2$  for the vector particle, we find the isoscalar form factor

$$F_K^S(s) = \frac{egc_V}{\sqrt{2}g_V} \frac{M_V^2}{M_V^2 - p^2}. \quad (4.27)$$

Plugging in the value of  $c_V$ ,

$$\begin{aligned} F_K^S(s) &= \frac{eg}{\sqrt{2}} \left( \frac{1}{g_\phi} \frac{M_\phi^2}{M_\phi^2 - s} - \frac{1}{\sqrt{2}g_\omega} \frac{M_\omega^2}{M_\omega^2 - s} \right) \\ &= -\frac{eg}{3g_\gamma} \left( \frac{M_\phi^2}{M_\phi^2 - s} + \frac{1}{2} \frac{M_\omega^2}{M_\omega^2 - s} \right) \\ &= \frac{c_\phi}{3} \frac{M_\phi^2}{M_\phi^2 - s} + \frac{c_\omega}{6} \frac{M_\omega^2}{M_\omega^2 - s}. \end{aligned} \quad (4.28)$$

In the last line, the constant factors and signs have been absorbed into the  $\phi$  and  $\omega$  couplings with the relation  $c_\phi = c_\omega = -eg/g_\gamma$ . The  $SU(3)$  prediction for these couplings is  $c_\phi = c_\omega = 1$  because of the ratio  $\omega : \phi = 3 : -3/\sqrt{2}$ . This form of the form factor is an approximation of the VMD model which works excellently at this level.

Since the vector particle under consideration here are resonance states and not stable particles, it is not

appropriate to continue using a stable particle propagator. Therefore, we replace it with a Breit-Wigner propagator whose general form is given by

$$\frac{i}{M_V^2 - q^2} \rightarrow \frac{i}{M_V^2 - q^2 + iq\Gamma_V}. \quad (4.29)$$

This replacement as shown in fig. 4.4 is for illustration only. For the analysis of the experimental data, we use the form of Breit-Wigner as given in [24],

$$\frac{i}{M_V^2 - q^2} \rightarrow \frac{i}{M_V^2 - s - i\sqrt{s}\Gamma_V(s)}, \quad (4.30)$$

where  $\Gamma_V(s)$  is the  $s$ -dependant width of the vector particle, discussed in chapter 5. We use the energy-dependant width only for  $\phi$  in the analysis of the timelike data since we concentrate only on the  $\phi$ -region. For the  $\omega$ , we use the full width since it only has a small residue in the  $\phi$  peak. In the spacelike region, vector particle decaying to kaons is kinematically forbidden. Therefore, the propagator is replaced with a simple function of the form

$$\frac{i}{M_V^2 - q^2} \rightarrow \frac{i}{M_V^2 - s}. \quad (4.31)$$

# Chapter 5

## Phenomenology

The model developed in the previous chapters is fit with data from various experiments in the spacelike and timelike region using the Python programming language. In this chapter, we first present the various datasets and fit functions used in the respective regions, and proceed to show the fits to the data and determine the  $\phi$ -meson parameters in addition to the  $\omega$  coupling.

### 5.1 Experimental Datasets

#### Spacelike Region

The data for the spacelike region ( $s < 0$ ) is obtained from [25, 26]. The experiments were done for  $eK$  scattering for charged kaons. Data is available only for charged kaons due to experimental constraints in producing neutral kaon beams.

The form factor data is fit with the expression

$$F_{K^+}(s) = \frac{c_\phi}{3} \frac{M_\phi^2}{M_\phi^2 - s} + \frac{c_\omega}{6} \frac{M_\omega^2}{M_\omega^2 - s} + \left( \frac{1}{2} - \frac{c_\phi}{3} - \frac{c_\omega}{6} \right) \frac{M_{\omega'}^2}{M_{\omega'}^2 - s} + F_K^V(s), \quad (5.1)$$

where the isovector part  $F_K^V(s)$  is obtained from eq. 3.14. The  $\omega' = \omega(1420)$  resonance is introduced to fix the isoscalar normalisation to 1/2. In this energy range, decay of the vector particles is energetically not possible. Therefore, the widths of these particle are set to zero for both the isoscalar and isovector resonances.

The spacelike region in comparison to a simple VMD model is shown in fig. 5.1. The red line is drawn with our fit results from the combined fit of of space- and timelike data, which will be discussed in section 5.2. The green line is drawn using the VMD model for both the isovector and isoscalar resonances. Our result agrees with the VMD picture to a great extent.

#### Neutral Kaon Charge Radius

The average value of the neutral kaon charged radius as quoted in [21] is

$$\langle r^2 \rangle = -0.077 \pm 0.010 \text{ fm}^2.$$

Experimental determination of the charged radius was done by neutral kaon decay  $K_{S,L} \rightarrow \pi^+ \pi^- e^+ e^-$  [27, 28]. Emission of a virtual photon takes place in this decay, as shown in fig. 5.2, via the  $CP$  conserving charge radius process among others. A  $K_L$  is transformed into a  $K_S$  by emission of a virtual

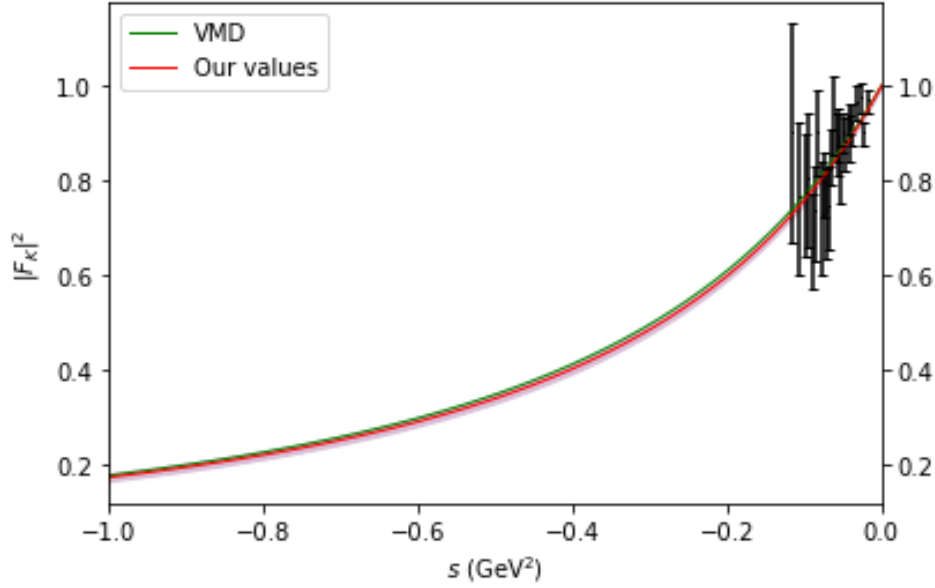


Figure 5.1: Extended plot of the spacelike region showing the comparison of our fit results from the combined space- and timelike fit of all the charged datasets, and the VMD picture for all the resonances. The black lines are the spacelike datasets, the red line is our average for the parameters, and the green line is the VMD results.

photon. This is followed by the decay of the  $K_S$  into  $\pi^+\pi^-$ . The virtual photon acts as a probe to the  $K^0$  and relates the charge radius coupling to the charge radius of the  $K^0$  [27]. Another determination of the charged radius of the neutral kaon was done by electronic regenerations [29, 30]. This was based on  $K^0$  elastically scattering off electrons, where the amplitude is proportional to the mean-squared charged radius of the  $K^0$  [31]. One theoretical calculation was done by using the dispersive method [8].

For the fit to the data, we use the relation

$$\langle r^2 \rangle = 6 \frac{dF(s)}{ds} \Big|_{s=0}. \quad (5.2)$$

For the isoscalar resonances, the Breit-Wigner relations can be analytically differentiated as

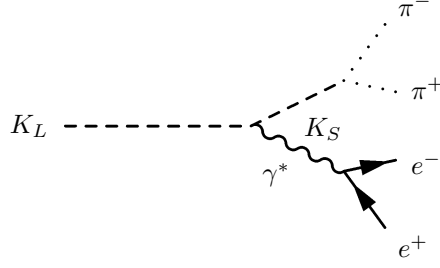
$$\frac{dF^S(s)}{ds} \Big|_{s=0} = \frac{c_\phi}{3} \frac{1}{M_\phi^2} + \frac{c_\omega}{6} \frac{1}{M_\omega^2} + \left( \frac{1}{2} - \frac{c_\phi}{3} - \frac{c_\omega}{6} \right) \frac{1}{M_{\omega'}^2}, \quad (5.3)$$

and the isovector part is obtained by numerically differentiating eq. (3.14) at  $s = 0$ .

## Timelike Region

Data in the timelike ( $s > 0$ ) region was obtained by  $e^+e^-$  annihilation into a pair of kaons. For the charged kaons, we took data from CMD2 [32], CMD3 [33], SND [34] and BaBar [35]. Some discrepancies in the cross-section values were observed between different datasets [36]. For example, a 5.5% difference was observed between the CMD3 and BaBar datasets, and an almost 11% difference between the CMD2 and CMD3 datasets. There is some discrepancy between BaBar and SND data as well. For the neutral kaons, we took data from CMD2 [37], CMD3 [38] and SND [34]. In the case of SND, there are two sets depending on the mode by which the kaons were detected, namely the charged and neutral modes. The charged mode is the detection of kaons by decay into charged pions, and the neutral mode is the detection via neutral pions. The experimental signature of these two modes is based on the number of



Figure 5.2: Diagram for  $K_{S,L} \rightarrow \pi^+ \pi^- e^+ e^-$ .

photons and charged particles detected in the final state.

The Born cross-section is defined by the relation [17]

$$\sigma^0(s) = \frac{\pi\alpha^2}{3s} \sigma_K^3 |F_K(s)|^2. \quad (5.4)$$

For charged kaons, the Sommerfeld-Gamov-Sakharov factor,

$$Z(s) = \frac{\pi\alpha}{\sigma_K} \frac{1 + \alpha^2/(4\sigma_K^2)}{1 - \exp(-\pi\alpha/\sigma_K)}, \quad (5.5)$$

is multiplied to the cross-section to account for the radiative corrections [17, 39]. The Gamow factor yields the exchange of Coulomb photons and resums it to all orders in  $\alpha$ . At the order we are concerned with in this work, photon exchange affects only the charged particles. Therefore, the Gamow factor does not apply to the neutral kaons. Here,  $\sigma_K = \sqrt{1 - 4m_K^2/s}$ , and the form factor is the combination of VMD and dispersion theory derived in previous chapters,

$$F_{K^{\pm/0}}(s) = \frac{c_\phi}{3} \frac{M_\phi^2}{M_\phi^2 - s - i\sqrt{s}\Gamma_\phi(s)} + \frac{c_\omega}{6} \frac{M_\omega^2}{M_\omega^2 - s - iM_\omega\Gamma_\omega} + \left(\frac{1}{2} - \frac{c_\phi}{3} - \frac{c_\omega}{6}\right) \frac{M_{\omega'}^2}{M_{\omega'}^2 - s - iM_{\omega'}\Gamma_{\omega'}} \pm F_K^V(s), \quad (5.6)$$

where  $F_K^V(s)$  is the isovector form factor from eq. (3.14). The widths of  $\omega$  and  $\omega'$  are fixed from [21]. The energy-dependant width of the  $\phi$  is defined in [24] as

$$\Gamma_\phi(s) = \sum_{K=K^+, K^0} \frac{\gamma_{\phi \rightarrow K\bar{K}}(s)}{\gamma_{\phi \rightarrow K\bar{K}}(M_\phi^2)} \Gamma'_{\phi \rightarrow K\bar{K}} + \frac{f_{\phi \rightarrow \pi\rho+3\pi}(s)}{f_{\phi \rightarrow \pi\rho+3\pi}(M_\phi^2)} \Gamma'_{\phi \rightarrow \pi\rho+3\pi}, \quad (5.7)$$

where  $\Gamma'$  is the fraction of the decay width of the corresponding process. We ignore the other decay channels of  $\phi$  as their contributions to the full decay width are very small. We include the  $\omega'$  in the form factor expression to fix the normalization to 1/2 at  $s = 0$ . Since we are only interested in the  $\phi$  region, we include only the next highest resonance for this purpose and leave out  $\phi' = \phi(1680)$  and other higher resonances. The difference in the fit results by inclusion of these higher resonances is negligible. The quantities  $\gamma(s)$  and  $f(s)$  are defined as [24]

$$\gamma_{\phi \rightarrow K\bar{K}}(s) = \frac{(s - 4M_K^2)^{3/2}}{s}, \quad (5.8)$$

$$f_{\phi \rightarrow \pi\rho+3\pi}(s) = \left( \frac{\lambda(M_\phi^2, M_\pi^2, M_\rho^2)}{s} \right)^{3/2},$$

and  $\lambda$  is the Källén function,

$$\lambda(a, b, c) = a^2 + b^2 + c^2 - 2ab - 2bc - 2ca. \quad (5.9)$$

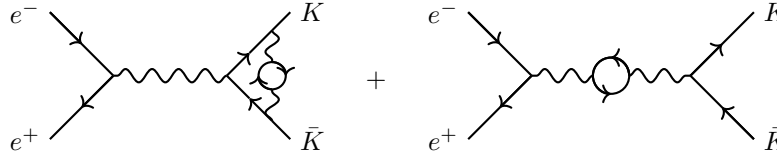


Figure 5.3: Vacuum polarisation contributions to kaon form factor.

## 5.2 Fits

The fits were done for all three bounds of the isovector part, the lower bound, central value and upper bound. We fit the theoretical values to the data in three ways; the combined fit of space- and timelike data, individual timelike fits, and another timelike fit with  $c_\omega = c_\phi$ . In the first two fits, the free parameters are the  $\phi$  coupling,  $\phi$  mass and width, and the  $\omega$  coupling. In the other timelike fit, the  $\phi$  parameters are free, but we assume the constraint  $c_\omega = c_\phi$ . All the other parameters such as the mass and width of  $\omega$  and higher resonances are fixed from [21]. The third fit is done to determine the contribution of the  $\omega$  in the spacelike region and around the  $\phi$  peak. The combined fit gives information about the contribution of the isovector form factor more prominently than the timelike fits, as the spacelike region is dominated by the isovector form factor.

### Removing Vacuum Polarization

Only CMD2 neutral and BaBar charged datasets had vacuum polarization (VP) removed from the cross-section data. For the other datasets, we removed the hadronic and leptonic vacuum polarizations, shown in fig. 5.3, using the Fortran routing from [40]. The code outputs the running fine structure constant  $\Delta\alpha(s)$ , which is related to the bare cross-section  $\sigma^0(s)$  and dressed cross-section  $\sigma(s)$  via

$$\sigma^0(s) = \sigma(s) |1 - \Delta\alpha(s)|^2. \quad (5.10)$$

Removal of VP led to a shift in the mass of  $\phi$  by about 0.26 MeV less than the PDG value, which is as expected [41].

### Systematic Uncertainty

Systematic uncertainties arise due to various factors such as detector efficiency, background effects, etc. These are fully or partially correlated uncertainties. Fully correlated errors include normalization uncertainties like detector efficiency and luminosity measurement. Such correlations lead to a bias in the fit because small data values get a smaller percentage of normalization uncertainty. This bias is the d'Agostini bias [42]. The chi-square minimization defined as

$$\chi^2 = \sum_{i,j} (f(x_i) - y_i) V(i,j)^{-1} (f(x_j) - y_j), \quad (5.11)$$

where  $f(x)$  is the fit function,  $y$  is the data and  $V$  is the covariance matrix, gets a lower value than expected due to the bias.

We follow the method presented in [43] which is a slight modification of the method suggested in [44]. It was observed that the normalization uncertainties must be closer to the true value rather than the measurement. The modified iterative covariance matrix is

$$V_{n+1}(i,j) = V^{stat}(i,j) + \frac{V^{syst}(i,j)}{y_i y_j} f_n(x_i) f_n(x_j), \quad (5.12)$$

where  $V^{stat}$  is the statistical covariance matrix, and  $V^{syst}$  is the systematic covariance matrix. An empirical covariance matrix, which is a linear sum of the statistical and systematic matrices, was used

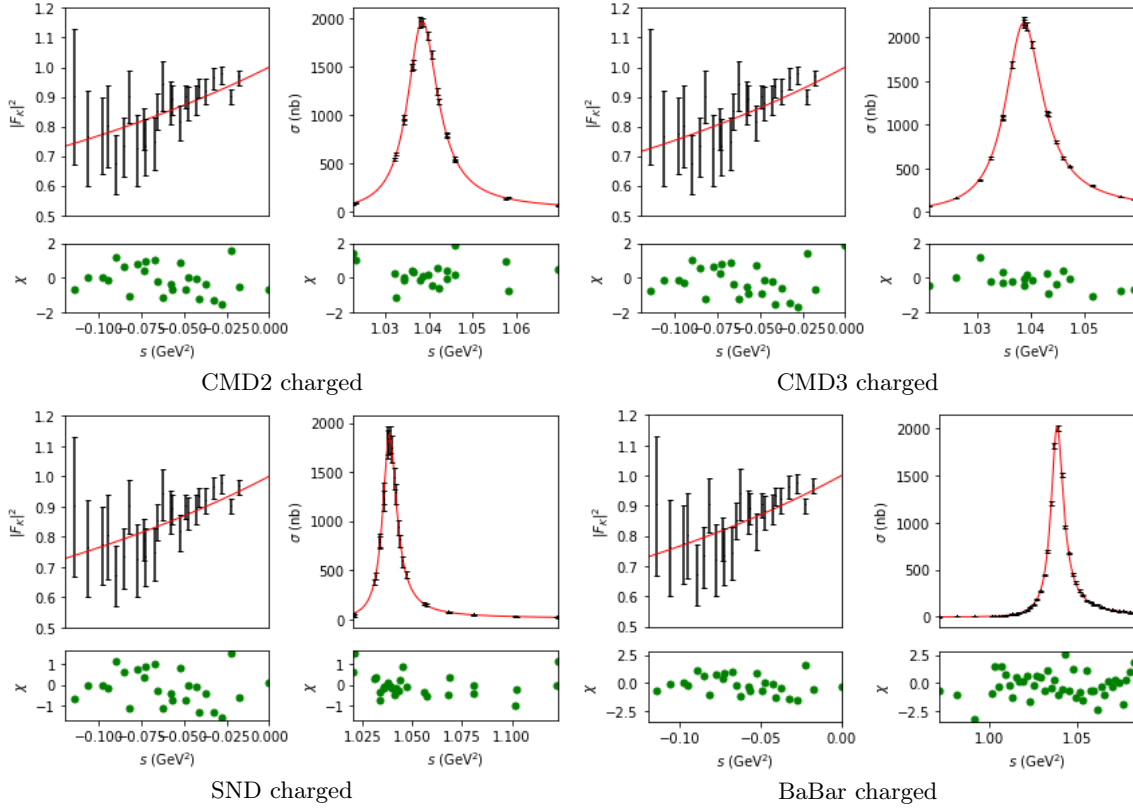


Figure 5.4: Fits of charged datasets in combination with spacelike data.

The left side of the graph shows the spacelike ( $s < 0$ ) region. The right side is the timelike ( $s > 0$ ) region. The bottom panel of the plots give the relative difference between the fit value and the actual data value divided by the standard deviation.

as the initial guess. In each iteration step, the fit function  $f(x)$  and the full covariance matrix  $V$  is updated. All the other quantities remain the same. The iterative values converge quickly to the final result for the covariance matrix in less than five iterations.

In the initial analysis, we did not include the systematic uncertainties and the errors were purely statistical. Inclusion of the systematic uncertainties lead to a slight increase in the  $\chi^2$  values. On the other hand,  $c_\phi$  and  $c_\omega$  values decreased slightly. There was negligible difference in  $M_\phi$  and  $\Gamma_\phi$  values.

### 5.3 Observations

The graphs of the combined space- and timelike fits are shown in figs. 5.4 and 5.5. The left side is the spacelike ( $s < 0$ ) region which is a combination of both the spacelike datasets, and also the neutral kaon charged radius (not shown in the plot). The right side is the timelike ( $s > 0$ ) region. The timelike datasets are fitted individually. The black lines are the data values from the respective experiments and the red line is our fit. The bottom panels on both sides indicate the ratio of the difference between the theoretical and experimental values, and the standard deviation, in green dots.

The fit results for the central isovector value is given in table B.1 and shown in fig. 5.6 for all three types of fits. The parameters from the combined fits are shown with blue lines and the timelike fit with red lines. The second timelike fit with fixed  $c_\omega$  is shown with green lines. Each parameter, including

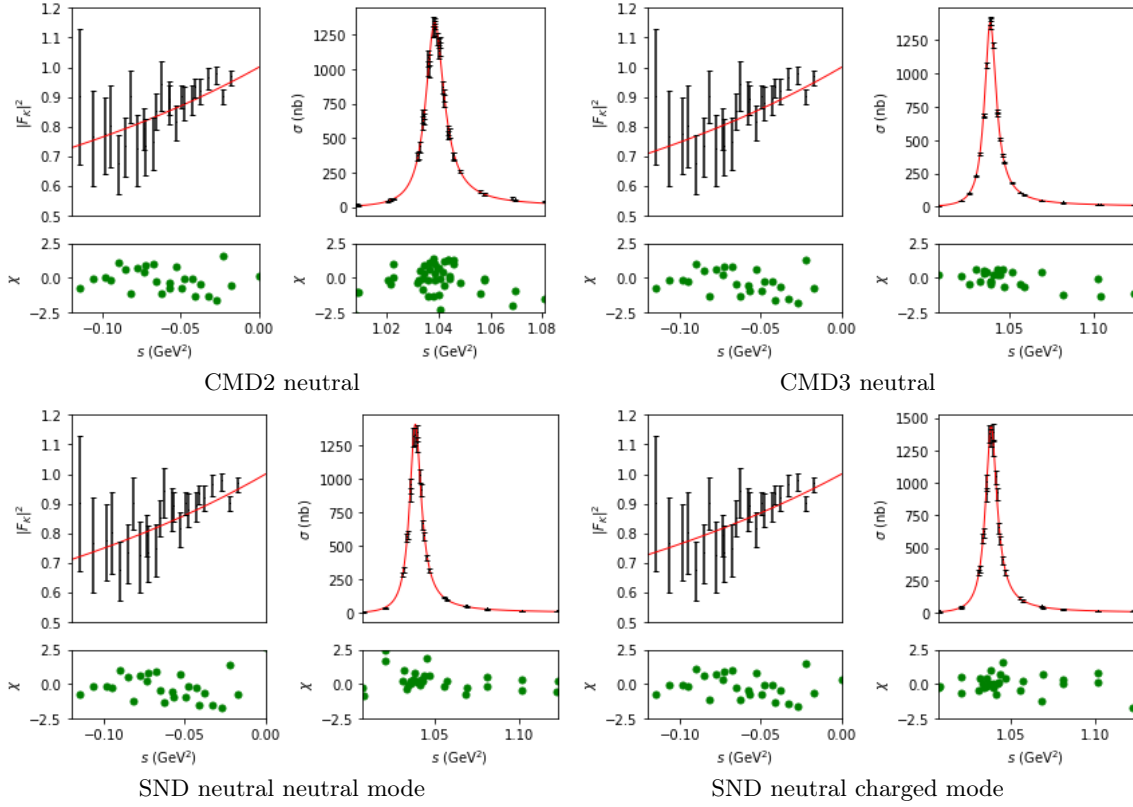


Figure 5.5: Fits of neutral datasets in combination with spacelike data.

The left side of the graph shows the spacelike ( $s < 0$ ) region. The right side is the timelike ( $s > 0$ ) region. The bottom panel of the plots give the relative difference between the fit value and the actual data value, divided by the standard deviation.

the  $\chi^2/dof$  values, is shown individually in different plots. The grey band indicates the expected value:

$$\begin{aligned} c_\phi &= 1, & M_\phi &= 1019.461 \pm 0.016 \text{ MeV}, \\ c_\omega &= 1, & \Gamma_\phi &= 4.249 \pm 0.013 \text{ MeV}. \end{aligned}$$

The comparison of the three bounds of the isovector part for the combined fit is shown in fig. 5.7. The isovector comparisons for the two timelike fits are shown in figs. 5.8 and 5.9. The upper isovector bound is represented by blue lines, the central value is red, and the lower bound is represented by the green lines. Each parameter is shown in a separate plot.

Overall, the  $\phi$  parameter values for all three fits are consistent with each other, as well as the expected values from the PDG to a great degree. However, the  $\omega$  coupling varies greatly between the combined and timelike fits. The combination with the spacelike data constrains the error in  $c_\omega$  to a smaller range. The  $\chi^2$  values are also in the acceptable range, although some datasets have a higher value. The overall difference in the  $\phi$  parameters for the three isovector bounds is negligible for all three fit-types. There is a significant difference in  $c_\omega$ , with the neutral and charged datasets showing shifts in opposite directions. The  $\chi^2$  values for the second timelike fit is higher than the other two fits indicating a significant  $\omega$  residue and isovector contribution.

As observed from fig. 5.6, the uncertainty bound of  $c_\omega$  is smaller when the timelike data is combined with the spacelike data. The full charged and neutral fits have similar values of  $c_\omega$  for both fit-types. The  $\chi^2$  values are also smaller for the combined fit than both the timelike fits in most datasets. The

$\chi^2$  values of the timelike fit with fixed  $c_\omega$  is higher than the other fits in general. The difference in the  $\phi$  parameters is not as significant as  $c_\omega$ . For the  $\phi$  coupling, the results of the neutral datasets fall into the expected value of 1 more than the charged datasets. The results of the mass and width of  $\phi$  agree with the experimental results obtained in the respective papers.

From fig. 5.7, we see that the three values of the isovector part has negligible effect on the  $\phi$ -meson parameters for combined fit of space- and timelike data. The upper bound values  $\phi$  coupling is bigger than the central and lower bound for the charged datasets, and smaller for the neutral datasets, but to a negligible effect ( $\sim 0.1\%$ ). In the case of the mass and width, the upper bound has a smaller value than the central and lower bounds. This difference is also negligible, of the order  $10^{-5}$  for mass and about  $0.14\%$  for width. The difference between the bounds is significant for the  $\omega$  coupling. For the neutral datasets, there is a positive shift for the upper isovector bound and negative for the lower bound, whereas a positive shift is observed for the lower bound in charged datasets and a negative shift of the upper bound. This difference in the charged and neutral datasets is expected because the charged datasets have isovector part added to the form factor and the neutral datasets have it subtracted. The average difference of the upper bound is about  $9.4\%$  and the lower bound is about  $9.3\%$  as compared to the central values. This difference is similar to the difference observed in the kaon isovector form factor.

In case of the timelike fits as shown in fig. 5.8, the difference in  $c_\omega$  is higher than the combined fits, being  $13.1\%$  for lower limit and  $14.6\%$  for the upper limit, and has a similar behaviour to the combined fits. The difference in the  $\phi$  parameters are negligible ( $<0.05\%$ ). The difference in the  $\chi^2$  values for the three isovector bounds is much less significant than the other two fits.

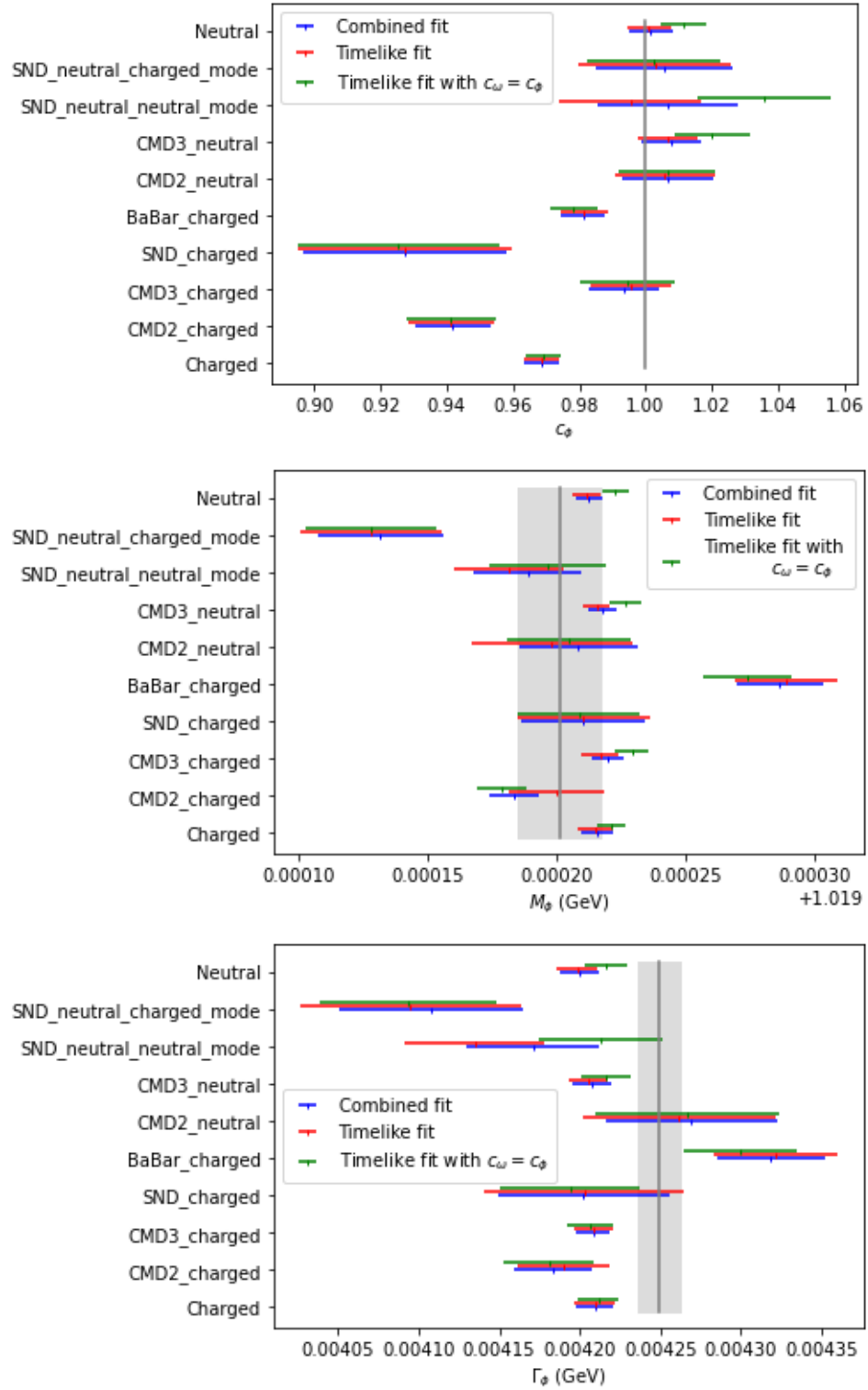
The difference in the  $\phi$  parameters is slightly more significantly observed in the other timelike fit with  $c_\omega = c_\phi$  shown in fig. 5.9. It is of about  $0.23\%$  in  $c_\phi$  and about  $0.18\%$  in  $\Gamma_\phi$ . The difference in  $M_\phi$  is negligible. The behaviour of the mass and width is opposite for the charged and neutral datasets than the other two fits. The  $\chi^2$  values are more significantly varying for the different bounds.

Combining all the charged datasets into one fit, and all the neutral datasets into another gave fairly good results, the parameters were similar to the individual fits. However, the full charged fit has a large  $\chi^2$  value, indicating some inconsistencies between the datasets.

We calculated the kaon charged radius by using the derived fit results of the central isovector values as given below:

| Fit                                   | $\langle r^2 \rangle_{K^0}$ (fm <sup>2</sup> ) | $\langle r^2 \rangle_{K^\pm}$ (fm <sup>2</sup> ) |
|---------------------------------------|--|--|
| Combined fit                          | $-0.073 \pm 0.003$                             | $0.349 \pm 0.007$                                |
| Timelike fit                          | $-0.072 \pm 0.009$                             | $0.350 \pm 0.013$                                |
| Timelike fit with $c_\phi = c_\omega$ | $-0.074 \pm 0.003$                             | $0.349 \pm 0.001$                                |

The expression eq. (5.3) was used for the isoscalar part and the isovector part was obtained numerically. The radius of the neutral kaon agrees well with the PDG average, but the charged kaon radius is off by several standard deviations. This deviation for the charged kaons was observed for the individual spacelike fit of the data from [25]. The individual fit of the data from [26] gave expected results. There seems to be some incompatibility in the former dataset, which was also noted in [8].



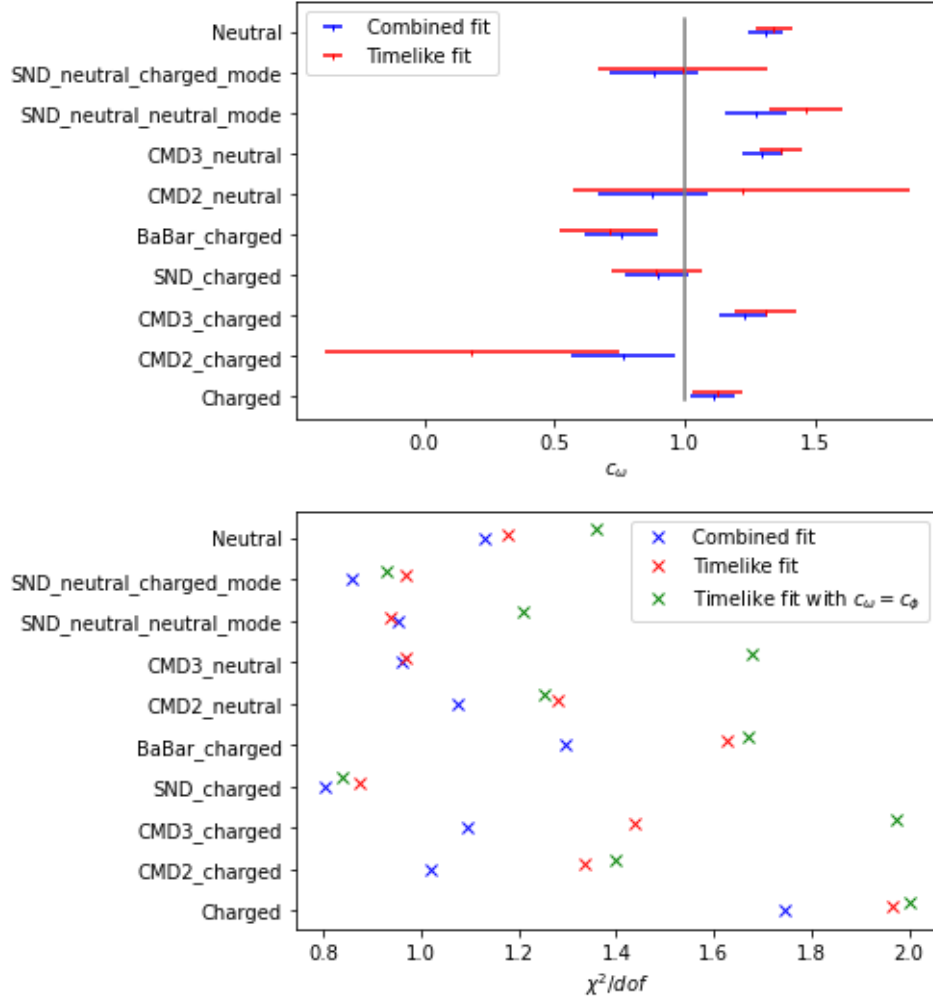
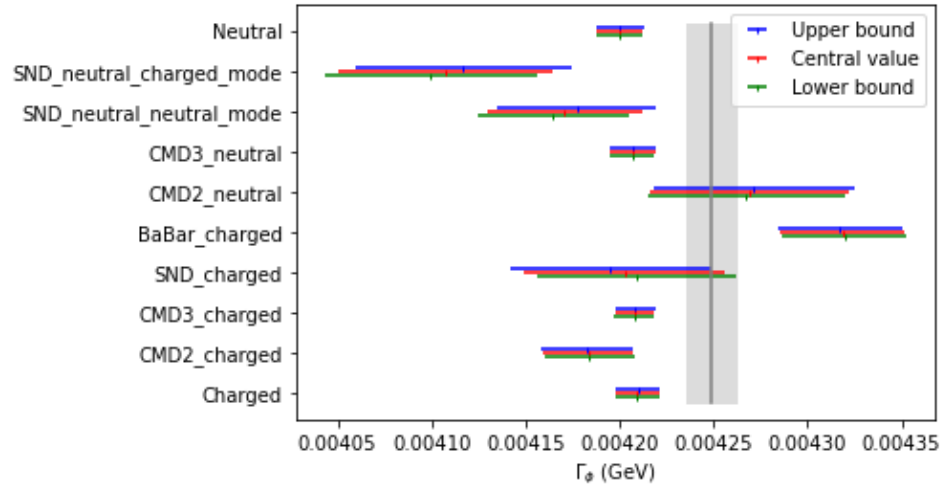
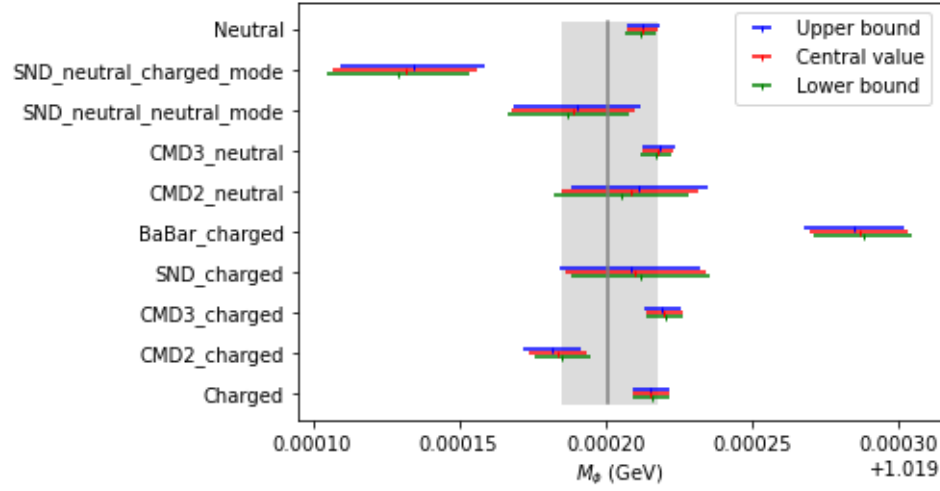
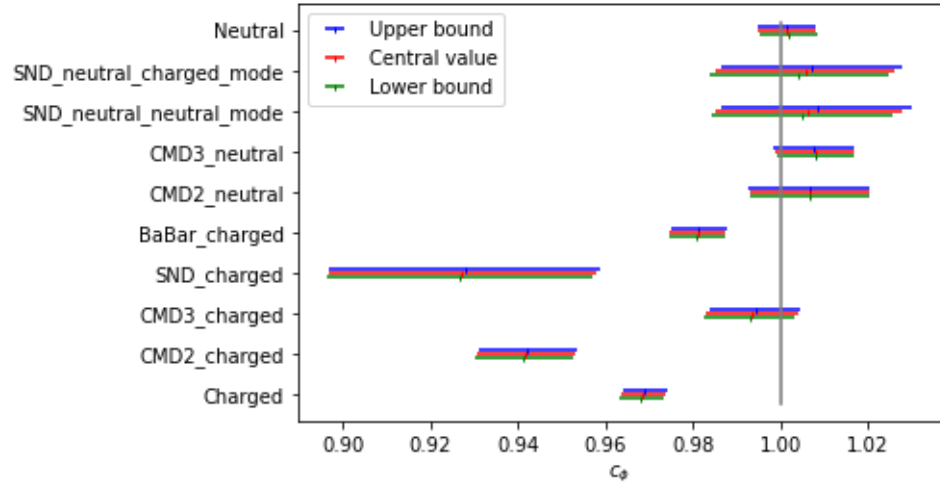


Figure 5.6: Results of fit for central isovector value.

The blue lines represent the combined space- and timelike fits. The individual timelike fits including  $c_\omega$  as a fit parameter is shown by the red line and the timelike fits where  $c_\omega$  was fixed is shown by the green lines. The first graph is the comparison of the  $\phi$ -coupling. The second and third graphs are the  $\phi$  mass and width for the different fits and experiments. The fourth graph is the  $\omega$  coupling. The grey lines denote the expected values of the parameters. The  $\chi^2/dof$  values for the fits are shown in the last graph.





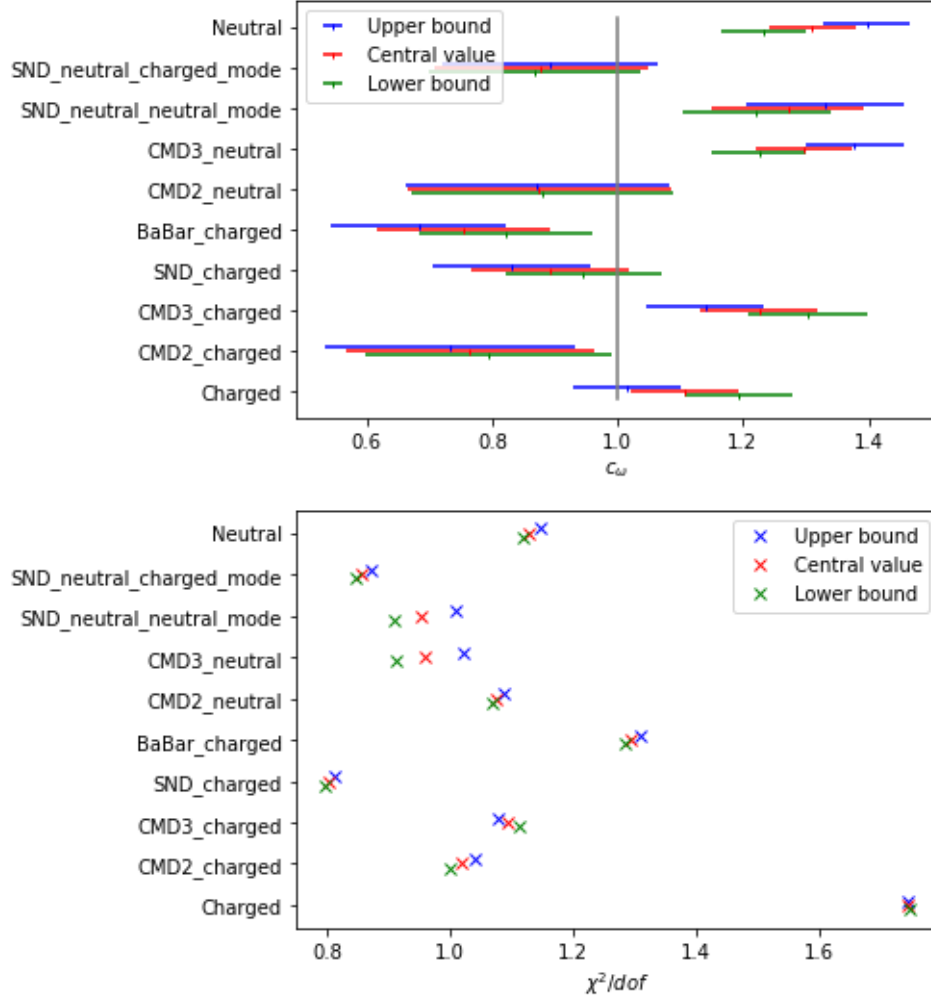
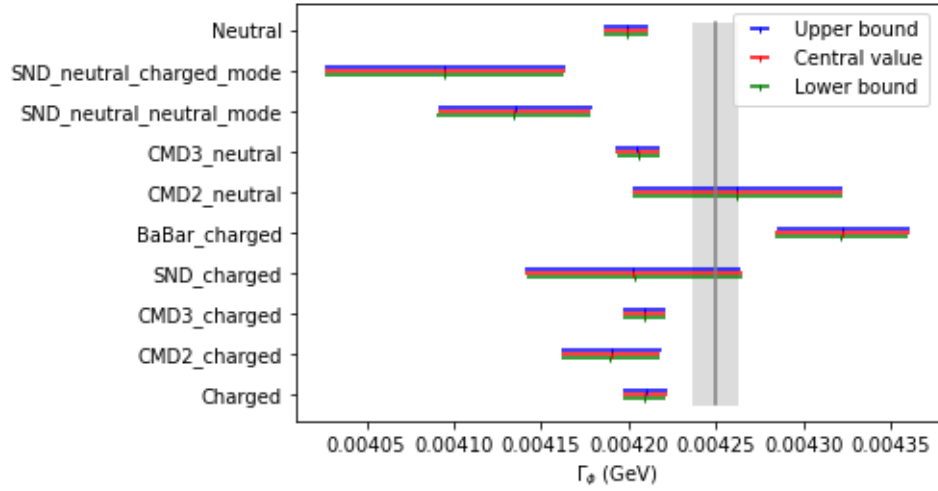
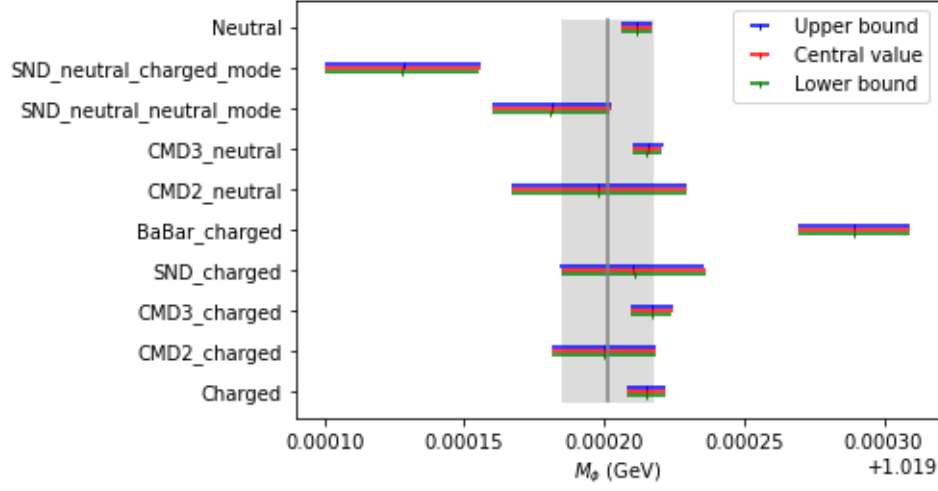
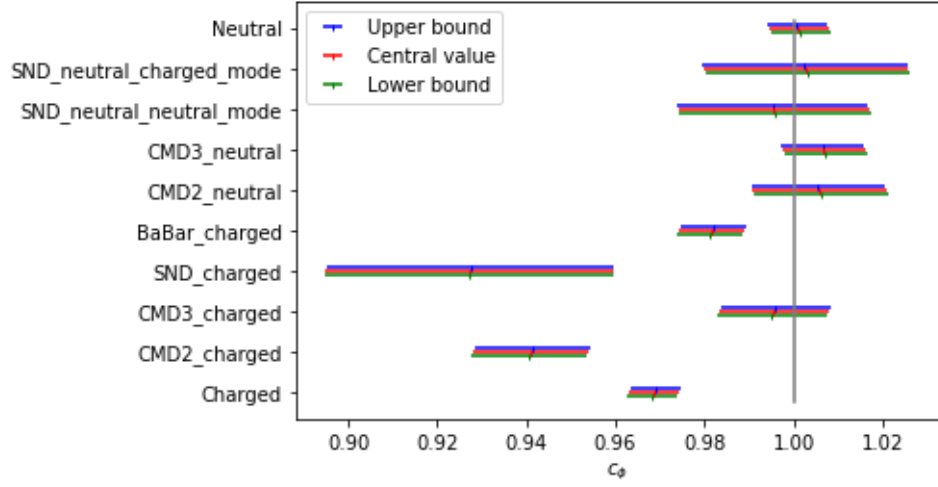


Figure 5.7: Comparison of the three isovector bounds for combined space- and timelike fit. The fits done with the central isovector values are represented by the red lines and the lower and upper bounds are shown by the green and blue lines, respectively. The first graph is the comparison of the  $\phi$ -coupling for each isovector bound for each experiment, second and third graphs are the  $\phi$  mass and width respectively, and the fourth graph is the  $\omega$ -coupling. The grey lines denote the expected values of the parameters. The last graph at the bottom is the  $\chi^2/dof$  values for all the fits.



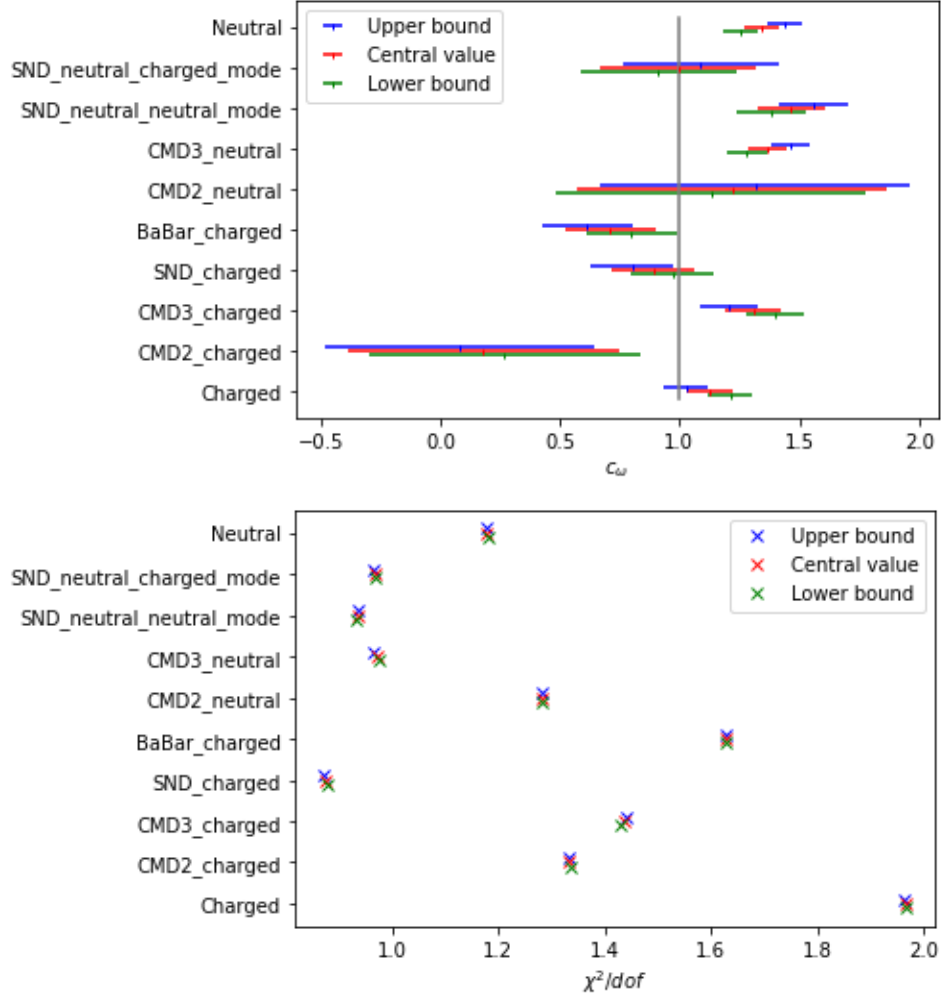
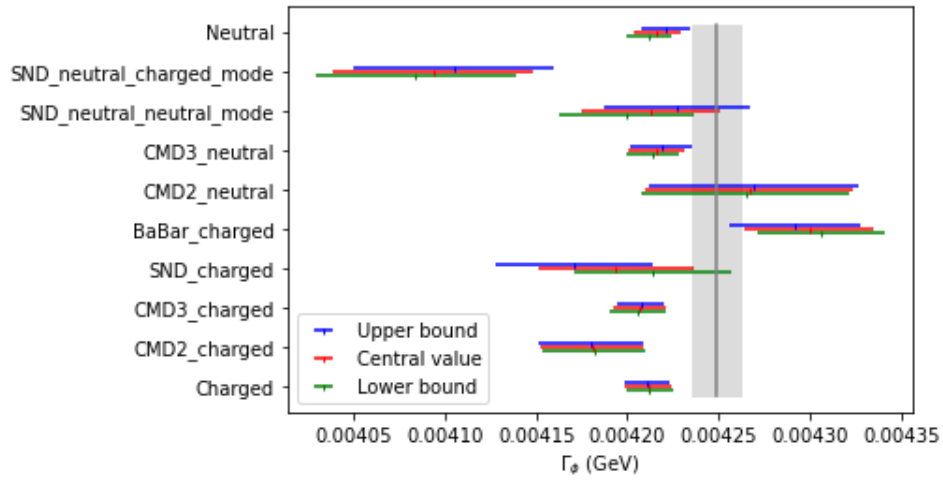
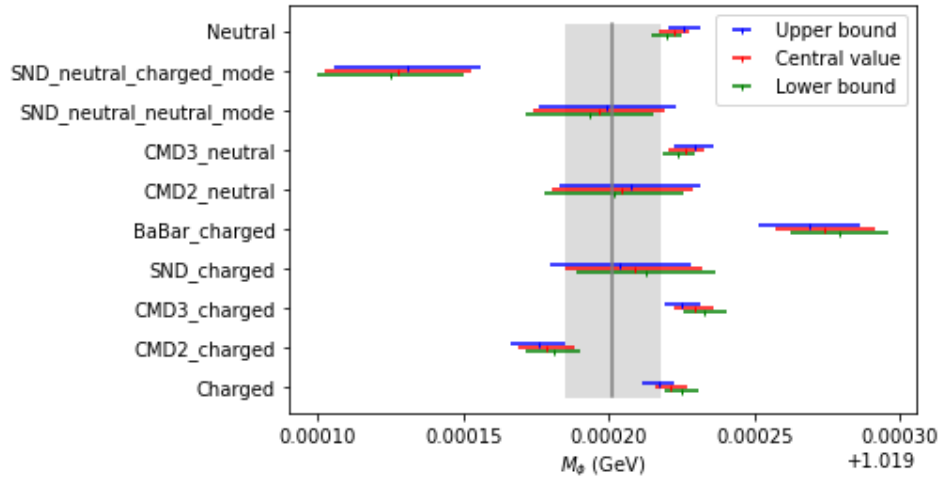
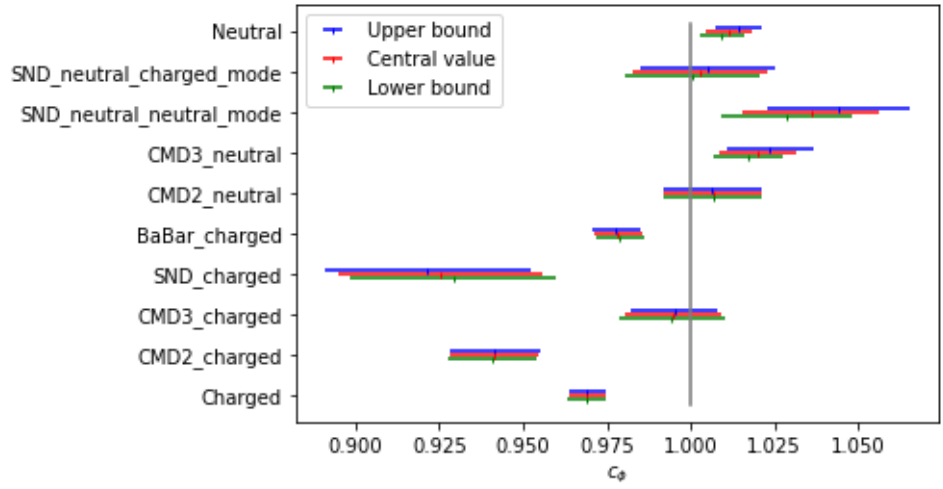


Figure 5.8: Comparison of the three isovector bounds for timelike fit with  $c_\omega$  as a free parameter in the fit.

The fits done with the central isovector values are represented by the red lines and the lower and upper bounds are shown by the green and blue lines, respectively. The first graph is the comparison of the  $\phi$ -coupling for each isovector bound for each experiment, second and third graphs are the  $\phi$  mass and width respectively, and the fourth graph is the  $\omega$ -coupling. The grey lines denote the expected values of the parameters. The last graph at the bottom is the  $\chi^2/\text{dof}$  values for all the fits.



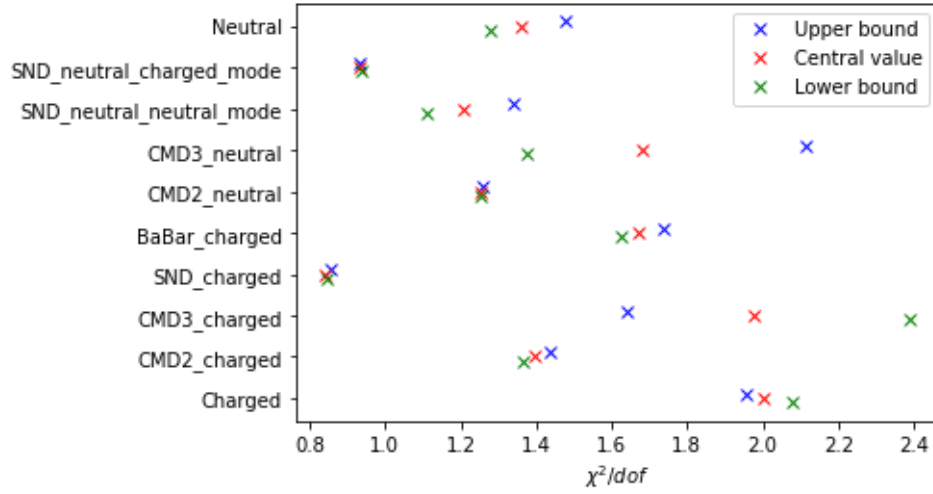


Figure 5.9: Comparison of the three isovector bounds for timelike fit with  $c_\omega = c_\phi$ .

The fits done with the central isovector values are represented by the red lines and the lower and upper bounds are shown by the green and blue lines, respectively. The first graph is the comparison of the  $\phi$ -coupling for each isovector bound for each experiment, second and third graphs are the  $\phi$  mass and width respectively. The grey lines denote the expected values of the parameters. The last graph at the bottom is the  $\chi^2/dof$  values for all the fits.

# Chapter 6

## Summary

In this thesis, we have derived an improved model for the electromagnetic kaon form factors. The isovector part of the form factor was derived via a dispersive framework with the pion form factor and the improved  $\pi\pi \rightarrow K\bar{K}$  scattering phase as input. The  $\rho$ -meson contribution was determined dispersively, and the  $\rho'$  was introduced with a Breit-Wigner formalism to account for the inelastic effects and normalization. We fixed the full isovector normalization to  $1/2$ . The phase of the  $\pi\pi \rightarrow K\bar{K}$  partial  $P$ -wave from [14] was the input for the pion vector form factor which rendered the imaginary part of the kaon isovector form factor real by construction. This input for the phase is a recent improved result (2020), as compared to the previous calculation done in [8] in the late 1970s. The uncertainty in the isovector region was also calculated. The relative difference in the isovector form factor of the upper and lower bounds in comparison to the central value falls within 10%. The isoscalar part of the form factor was determined from the Lagrangian given in [9] which led to the  $SU(3)$ -symmetric approximation of the vector meson dominance model. Here we considered the dominant  $\phi$  and  $\omega$  resonance states, and an additional  $\omega'$  was introduced to fix the normalization to  $1/2$ . We then proceeded to phenomenologically determine the  $\omega$  coupling and  $\phi$ -meson parameters by fits to several datasets in the timelike region around the  $\phi$  resonance, and data in the spacelike region. The fits were done for combined space- and timelike data, individual timelike data, and also an additional timelike fit but with fixed  $c_\omega = c_\phi$  to determine the amount  $\omega$  and isovector contribution. Using the weighting procedure in [21] for uncorrelated data, the average values of the parameters from all the fits and for all three isovector bounds is given in table 6.1.

The  $\phi$  and  $\omega$  couplings fall into the expected  $SU(3)$  values of  $c_\phi = c_\omega = 1$  within the uncertainty band. The  $\phi$  width is also close to the PDG average. The  $\phi$  mass has shifted to a lower value by about 0.26 MeV as compared to the PDG, which is expected because we removed the vacuum polarization [41] using the routine from [40]. It was observed that the uncertainty band of  $c_\omega$  was significantly smaller for the combined fits than the timelike fit. The difference in the  $\phi$ -meson parameters was significantly less. The  $\chi^2$  values for the combined fit was also found to be more reasonable than the timelike fits, with the timelike fit with fixed  $c_\omega$  being the largest. The difference between the upper and lower bounds with the central isovector value in  $c_\omega$  was calculated to be about 10% for the combined fits and 14% for the timelike fits. The difference in the  $\phi$  parameters are negligible. The upper and lower bounds show opposite behaviour in the direction of shift compared to the central value, most significantly for  $c_\omega$ . This difference in the direction of shift is expected because the isovector form factor is added for charged kaons and subtracted for neutral kaons.

| Fit                                   | $c_\phi$          | $M_\phi$ (MeV)       | $\Gamma_\phi$ (MeV) | $c_\omega$        |
|---------------------------------------|-------------------|----------------------|---------------------|-------------------|
| Combined fit                          | $0.984 \pm 0.004$ | $1019.214 \pm 0.003$ | $4.207 \pm 0.004$   | $1.158 \pm 0.037$ |
| Timelike fit                          | $0.984 \pm 0.004$ | $1019.214 \pm 0.003$ | $4.206 \pm 0.004$   | $1.254 \pm 0.039$ |
| Timelike fit with $c_\omega = c_\phi$ | $0.987 \pm 0.004$ | $1019.220 \pm 0.003$ | $4.212 \pm 0.004$   | –                 |

Table 6.1: Average values of parameters from all the three isovector bounds of all the fits.

The best fit is the combined space- and timelike fit for the central isovector values:

$$\begin{aligned}
c_\phi &= 0.992 \pm 0.006, \\
M_\phi &= 1019.219 \pm 0.008 \text{ MeV}, \\
\Gamma_\phi &= 4.211 \pm 0.012 \text{ MeV}, \\
c_\omega &= 1.130 \pm 0.083.
\end{aligned}$$

We excluded the result of the CMD2 charged dataset in the above average as it has the most deviation from  $c_\phi = 1$ , and leads to a large  $\chi^2$  value. The combined charged and neutral fits are also excluded.

The charged radius of neutral kaons calculated using the fit results agreed with the PDG average to a great extent. But the radius of the charged kaons was off by several standard deviations. This was also observed for the individual spacelike fit of the data from [25], indicating that the data from [25] is somehow incompatible. This incompatibility was also noticed in [8]. The result from the fit of [26] agreed with the PDG average.

We can infer from the overall fit results that there is a significant  $\omega$  residue in the  $\phi$  region, and therefore allowing the  $\omega$  coupling be a free parameter gives slightly better fit results. The results of  $c_\omega$  and  $\chi^2$  is better for the combined space- and timelike fits which may be because of the significant isovector dominance in the spacelike region.

Calculation of the electromagnetic kaon form factors has a wide range of applications in particle physics. It could be used to constrain the  $K\bar{K}$  HVP in the determination of the  $g - 2$  of the muon. HVP calculation requires analysis beyond the  $\phi$  region in addition to what has been done in this project. Another contribution to  $(g - 2)_\mu$  is of the spacelike charged kaon form factor to the HLbL kaon box diagram. This calculation was previously done using the pure VMD model [36]. The kaon form factors can also be used to determine the electromagnetic kaon mass difference via the diagram shown in fig. 6.1. The mass difference is proportional to the product of the isoscalar and isovector form factors, integrated over spacelike arguments. This has implications in corrections to Dashen's theorem [45], which states that in the chiral  $SU(3)$  limit, the squared difference in the electromagnetic mass of the pseudoscalars  $\pi^{\pm,0}, K^{\pm,0}$  is equal:

$$(M_{\pi^\pm}^2 - M_{\pi^0}^2) = (M_{K^\pm}^2 - M_{K^0}^2). \quad (6.1)$$

Studying kaon observables in comparison with pions gives an insight about  $SU(3)$  flavour-breaking in QCD [46]. Kaon electromagnetic form factor is sensitive to many such observables. It also contains information about the structure of hadrons.

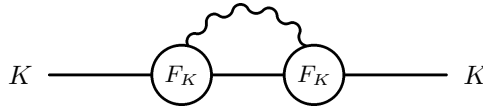


Figure 6.1: Diagram of kaon self energy, used to calculate the kaon mass difference.

# Appendix A

## Kinematics

### Phase Space Analysis

Consider the integral from the first line of eq. (3.5). It can be written as

$$\begin{aligned} I &= \int d^4 k_1 d^4 k_2 \delta(k_1^2 - m_\pi^2) \delta(k_2^2 - m_\pi^2) f(k_1, k_2) \\ &= \int d^3 k_1 d k_1^0 d^3 k_2 d k_2^0 \delta(k_1^2 - m_\pi^2) \delta(k_2^2 - m_\pi^2) f(k_1, k_2). \end{aligned} \quad (\text{A.1})$$

We use the relation

$$\delta(a - b) = \delta(x - y) \frac{dx}{da} \quad (\text{A.2})$$

to change the variables in A.1 to

$$\begin{aligned} \delta(k_1^2 - m_\pi^2) &= \frac{\delta(k_1^0 - \sqrt{\mathbf{k}_1^2 + m_\pi^2})}{2\sqrt{\mathbf{k}_1^2 + m_\pi^2}}, \\ \delta(k_2^2 - m_\pi^2) &= \delta((p - k_1)^2 - m_\pi^2) = \frac{\delta(\mathbf{k}_1 - \mathbf{k}_{cm})}{2\mathbf{k}_1}, \end{aligned} \quad (\text{A.3})$$

where we use conservation of four-momentum to say  $k_2 = p - k_1$ . Moving to the spherical coordinates and employing the delta functions, we get

$$\begin{aligned} I &= \int d\mathbf{k}_1 k_1^2 d\Omega \frac{1}{2\sqrt{\mathbf{k}_1^2 + m_\pi^2}} \frac{\delta(\mathbf{k}_1 - \mathbf{k}_{cm})}{2\mathbf{k}_1} f(k_1, k_2) \\ &= \frac{k_{cm}}{4\sqrt{k_{cm}^2 + m_\pi^2}} \int d\Omega f(k_1, k_2) \\ &= \frac{\sigma_\pi}{4} \int d\Omega f(k_1, k_2). \end{aligned} \quad (\text{A.4})$$

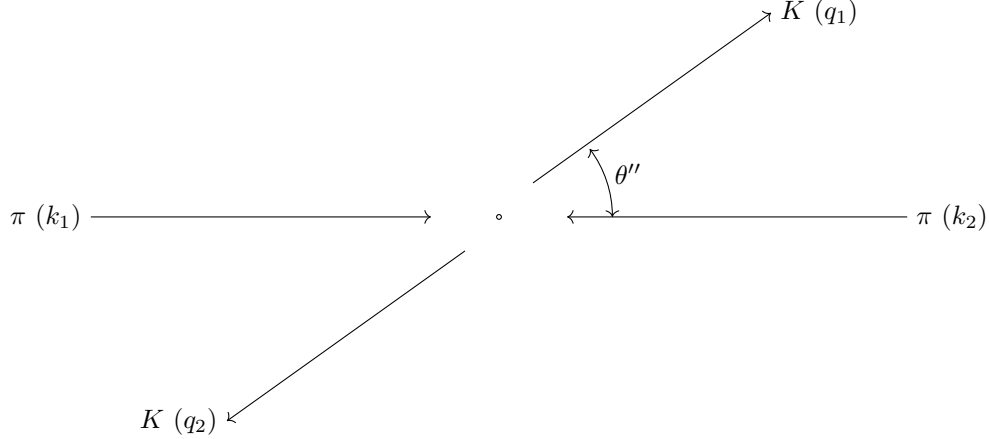
In the last line, we use  $k_{cm} = \sqrt{s}\sigma_\pi/2$  where  $\sigma_\pi = \sqrt{1 - 4m_\pi^2/s}$  is the center of mass cross-section of the pion intermediate states.



## Center-of-Mass Frame Kinematics

The center-of-mass frame relations are

$$\begin{aligned}
 k_1^0 &= k_2^0 = \frac{p^0}{2} = \frac{\sqrt{s}}{2}, \\
 \mathbf{k}_1 &= \mathbf{k}_2 = \frac{\mathbf{p}}{2} = \frac{\sqrt{s}\sigma_\pi}{2}, \\
 q_1 k_1 &= \frac{s}{4}(1 + \sigma_\pi \sigma_K \cos\theta''), \\
 q_2 k_1 &= \frac{s}{4}(1 - \sigma_\pi \sigma_K \cos\theta'').
 \end{aligned} \tag{A.5}$$



Consider the integral on the right hand side of eq. (3.5). We make the ansatz

$$\int d\Omega z'' (2k_1 - p)_\mu = L_1 (q_1 + q_2)_\mu + L_2 (q_1 - q_2)_\mu. \tag{A.6}$$

Contraction with  $(q_1 - q_2)^\mu$  on both sides of eq. (A.6) leads to:

$$\begin{aligned}
 \int d\Omega z'' (2k_1 - p)_\mu (q_1 - q_2)^\mu &= L_1 (q_1 + q_2)_\mu (q_1 - q_2)^\mu + L_2 (q_1 - q_2)_\mu (q_1 - q_2)^\mu \\
 \int d\Omega z'' [2k_1 \cdot (q_1 - q_2) - p \cdot (q_1 - q_2)] &= L_1 (q_1^2 - q_2^2) + L_2 (q_1 - q_2)^2 \\
 \int d\Omega z'' 2k_1 \cdot (q_1 - q_2) &= L_2 4q_K^2 \\
 \int d\Omega z'' s \sigma_\pi \sigma_K \cos\theta'' &= L_2 s \sigma_K^2,
 \end{aligned}$$

where we use the conservation of momentum  $p = q_1 + q_2$  and  $z'' = \cos\theta''$ . Therefore, we find

$$L_2 = \int d\Omega (z'')^2 \frac{\sigma_\pi}{\sigma_K}. \tag{A.7}$$

Now we contract  $(q_1 + q_2)^\mu$  on the both sides of eq. (A.6):

$$\begin{aligned}
 \int d\Omega z'' (2k_1 - p)_\mu (q_1 + q_2)^\mu &= L_1 (q_1 + q_2)_\mu (q_1 + q_2)^\mu + L_2 (q_1 - q_2)_\mu (q_1 + q_2)^\mu \\
 \int d\Omega z'' [2k_1 \cdot (q_1 + q_2) - p \cdot (q_1 + q_2)] &= L_1 (q_1 + q_2)^2 + L_2 (q_1^2 - q_2^2) \\
 \int d\Omega z'' [s - p \cdot p] &= L_1 p \cdot p \\
 0 &= L_1 s.
 \end{aligned}$$

Then,

$$L_1 = 0. \tag{A.8}$$

Plugging the result of  $L_1$  and  $L_2$  back into the ansatz eq. (A.6), we get

$$\begin{aligned} \int d\Omega \, z'' (2k_1 - p)_\mu &= \int d\Omega \, (z'')^2 \frac{\sigma_\pi}{\sigma_K} (q_1 - q_2)_\mu \\ &= \frac{\sigma_\pi}{\sigma_K} (q_1 - q_2)_\mu (2\pi) \int_{-1}^1 dz'' (z'')^2 \\ &= \frac{4\pi}{3} \frac{\sigma_\pi}{\sigma_K} (q_1 - q_2)_\mu. \end{aligned} \tag{A.9}$$

# Appendix B

## Fits

| Experiment               | $c_\phi$          | $M_\phi$ (MeV)       | $\Gamma_\phi$ (MeV) | $c_\omega$        | $\chi^2/\text{dof}$ |
|--------------------------|-------------------|----------------------|---------------------|-------------------|---------------------|
| Combined Charged         | $0.969 \pm 0.005$ | $1019.216 \pm 0.006$ | $4.210 \pm 0.012$   | $1.108 \pm 0.086$ | 1.746               |
| CMD2 charged             | $0.942 \pm 0.011$ | $1019.184 \pm 0.009$ | $4.183 \pm 0.024$   | $0.764 \pm 0.198$ | 1.018               |
| CMD3 charged             | $0.994 \pm 0.010$ | $1019.220 \pm 0.006$ | $4.208 \pm 0.010$   | $1.225 \pm 0.093$ | 1.094               |
| SND charged              | $0.927 \pm 0.031$ | $1019.210 \pm 0.024$ | $4.202 \pm 0.053$   | $0.892 \pm 0.125$ | 0.802               |
| BaBar charged            | $0.981 \pm 0.006$ | $1019.287 \pm 0.017$ | $4.319 \pm 0.033$   | $0.755 \pm 0.138$ | 1.295               |
| CMD2 neutral             | $1.007 \pm 0.014$ | $1019.208 \pm 0.023$ | $4.269 \pm 0.053$   | $0.875 \pm 0.210$ | 1.077               |
| CMD3 neutral             | $1.008 \pm 0.009$ | $1019.218 \pm 0.005$ | $4.207 \pm 0.012$   | $1.297 \pm 0.076$ | 0.959               |
| SND neutral neutral mode | $1.006 \pm 0.021$ | $1019.189 \pm 0.021$ | $4.171 \pm 0.041$   | $1.272 \pm 0.121$ | 0.953               |
| SND neutral charged mode | $1.006 \pm 0.020$ | $1019.131 \pm 0.024$ | $4.108 \pm 0.057$   | $0.878 \pm 0.170$ | 0.856               |
| Combined Neutral         | $1.002 \pm 0.006$ | $1019.213 \pm 0.005$ | $4.200 \pm 0.012$   | $1.310 \pm 0.069$ | 1.130               |

Fit results for combined fit of space and timelike data

| Experiment               | $c_\phi$          | $M_\phi$ (MeV)       | $\Gamma_\phi$ (MeV) | $c_\omega$        | $\chi^2/\text{dof}$ |
|--------------------------|-------------------|----------------------|---------------------|-------------------|---------------------|
| Combined Charged         | $0.969 \pm 0.005$ | $1019.215 \pm 0.007$ | $4.209 \pm 0.012$   | $1.124 \pm 0.094$ | 1.966               |
| CMD2 charged             | $0.941 \pm 0.013$ | $1019.199 \pm 0.018$ | $4.190 \pm 0.028$   | $0.180 \pm 0.565$ | 1.334               |
| CMD3 charged             | $0.996 \pm 0.012$ | $1019.217 \pm 0.007$ | $4.201 \pm 0.012$   | $1.307 \pm 0.119$ | 1.436               |
| SND charged              | $0.927 \pm 0.032$ | $1019.210 \pm 0.026$ | $4.203 \pm 0.062$   | $0.891 \pm 0.171$ | 0.873               |
| BaBar charged            | $0.981 \pm 0.007$ | $1019.289 \pm 0.020$ | $4.322 \pm 0.038$   | $0.710 \pm 0.189$ | 1.628               |
| CMD2 neutral             | $1.006 \pm 0.015$ | $1019.198 \pm 0.031$ | $4.262 \pm 0.060$   | $1.218 \pm 0.647$ | 1.281               |
| CMD3 neutral             | $1.007 \pm 0.009$ | $1019.215 \pm 0.005$ | $4.205 \pm 0.012$   | $1.367 \pm 0.083$ | 0.970               |
| SND neutral neutral mode | $0.996 \pm 0.021$ | $1019.181 \pm 0.021$ | $4.135 \pm 0.044$   | $1.466 \pm 0.142$ | 0.935               |
| SND neutral charged mode | $1.003 \pm 0.023$ | $1019.128 \pm 0.028$ | $4.095 \pm 0.068$   | $0.995 \pm 0.326$ | 0.967               |
| Combined Neutral         | $1.001 \pm 0.007$ | $1019.212 \pm 0.005$ | $4.199 \pm 0.013$   | $1.342 \pm 0.072$ | 1.178               |

Fit results of timelike data

| Experiment               | $c_\phi$          | $M_\phi$ (MeV)       | $\Gamma_\phi$ (MeV) | $\chi^2/\text{dof}$ |
|--------------------------|-------------------|----------------------|---------------------|---------------------|
| Combined Charged         | $0.969 \pm 0.006$ | $1019.221 \pm 0.006$ | $4.211 \pm 0.012$   | 2.002               |
| CMD2 charged             | $0.941 \pm 0.013$ | $1019.179 \pm 0.010$ | $4.181 \pm 0.028$   | 1.397               |
| CMD3 charged             | $0.995 \pm 0.014$ | $1019.229 \pm 0.007$ | $4.207 \pm 0.014$   | 1.975               |
| SND charged              | $0.925 \pm 0.030$ | $1019.209 \pm 0.024$ | $4.194 \pm 0.043$   | 0.840               |
| BaBar charged            | $0.978 \pm 0.007$ | $1019.274 \pm 0.017$ | $4.300 \pm 0.035$   | 1.669               |
| CMD2 neutral             | $1.007 \pm 0.015$ | $1019.204 \pm 0.024$ | $4.267 \pm 0.057$   | 1.253               |
| CMD3 neutral             | $1.020 \pm 0.011$ | $1019.226 \pm 0.006$ | $4.216 \pm 0.015$   | 1.679               |
| SND neutral neutral mode | $1.036 \pm 0.020$ | $1019.196 \pm 0.022$ | $4.213 \pm 0.038$   | 1.209               |
| SND neutral charged mode | $1.003 \pm 0.020$ | $1019.128 \pm 0.025$ | $4.094 \pm 0.055$   | 0.931               |
| Combined Neutral         | $1.012 \pm 0.007$ | $1019.223 \pm 0.005$ | $4.216 \pm 0.013$   | 1.361               |

Fit results of timelike data with  $c_\omega = c_\phi$ 

Table B.1: Fit results for central isovector values.

# Bibliography

- [1] F. Halzen and A. D. Martin. *Quarks and Leptons: An Introductory Course In Modern Particle Physics*. Wiley, 1984. ISBN: 978-0-471-88741-6.
- [2] P. A. M. Dirac. “The quantum theory of electron. Part II”. In: *Proc. Roy. Soc. Lond. A* 118 (1928), p. 351. DOI: 10.1098/rspa.1928.0056.
- [3] J. Schwinger. “On quantum electrodynamics and the magnetic moment of the electron”. In: *Phys. Rev.* 73 (4 Feb. 1948), pp. 416–417. DOI: 10.1103/PhysRev.73.416.
- [4] A. Keshavarzi, D. Nomura, and T. Teubner. “ $g - 2$  of charged leptons,  $\alpha(M_Z^2)$ , and the hyperfine splitting of muonium”. In: *Phys. Rev. D* 101.1 (2020), p. 014029. DOI: 10.1103/PhysRevD.101.014029. arXiv: 1911.00367 [hep-ph].
- [5] B. Abi et al. “Measurement of the Positive Muon Anomalous Magnetic Moment to 0.46 ppm”. In: *Phys. Rev. Lett.* 126.14 (2021), p. 141801. DOI: 10.1103/PhysRevLett.126.141801. arXiv: 2104.03281 [hep-ex].
- [6] G. W. Bennett et al. “Final Report of the Muon E821 Anomalous Magnetic Moment Measurement at BNL”. In: *Phys. Rev. D* 73 (2006), p. 072003. DOI: 10.1103/PhysRevD.73.072003. arXiv: hep-ex/0602035.
- [7] K. I. Beloborodov, V. P. Druzhinin, and S. I. Serednyakov. “Isoscalar and Isovector Kaon Form Factors from  $e^+e^-$  and  $\tau$  Data”. In: *J. Exp. Theor. Phys.* 129.3 (2019), pp. 386–390. DOI: 10.1134/S1063776119080016. arXiv: 1902.02474 [hep-ph].
- [8] S. Blatnik, J. Stahov, and C. B. Lang. “The Isovector Part of the Kaon Form-factor and the Kaon Charge Radii”. In: *Lett. Nuovo Cim.* 24 (1979), p. 39. DOI: 10.1007/BF02725742.
- [9] F. Klingl, Norbert Kaiser, and W. Weise. “Effective Lagrangian approach to vector mesons, Their structure and decays”. In: *Z. Phys. A* 356 (1996), pp. 193–206. DOI: 10.1007/s002180050167. arXiv: hep-ph/9607431.
- [10] R. J. Eden et al. *The Analytic S-Matrix*. Cambridge Univ. Press, 1966. ISBN: 978-0-521-52336-3.
- [11] R. E. Cutkosky. “Singularities and discontinuities of feynman amplitudes”. In: *J. Math. Phys.* 1 (1960), pp. 429–433. DOI: 10.1063/1.1703676.
- [12] K. M. Watson. “Some General Relations between the Photoproduction and Scattering of  $\pi$  Mesons”. In: *Phys. Rev.* 95 (1 July 1954), pp. 228–236. DOI: 10.1103/PhysRev.95.228.
- [13] R. Omnes. “On the Solution of certain singular integral equations of quantum field theory”. In: *Nuovo Cim.* 8 (1958), pp. 316–326. DOI: 10.1007/BF02747746.

- [14] J. R. Peláez and A. Rodas. “Dispersive  $\pi K \rightarrow \pi K$  and  $\pi\pi \rightarrow K\bar{K}$  mmplitudes from scattering data, threshold parameters and the lightest strange resonance  $\kappa$  or  $K_0^*(700)$ ”. In: (Oct. 2020). arXiv: 2010.11222 [hep-ph].
- [15] S. Holz. “Analyse des  $\eta'$  Übergangsformfaktors”. BA Thesis. Universität Bonn, 2016.
- [16] B. Aubert et al. “Precise measurement of the  $e^+e^- \rightarrow \pi^+\pi^-(\gamma)$  cross section with the initial state radiation method at BABAR”. In: *Phys. Rev. Lett.* 103 (23 Dec. 2009), p. 231801. DOI: 10.1103/PhysRevLett.103.231801. arXiv: 1205.2228 [hep-ex].
- [17] S. Fang, B. Kubis, and A. Kupść. “What can we learn about light-meson interactions at electron-positron colliders?” In: *Progress in Particle and Nuclear Physics* 120 (June 2021), p. 103884. DOI: 10.1016/j.pnpnp.2021.103884. arXiv: 2102.05922 [hep-ph].
- [18] S. P. Schneider, B. Kubis, and F. Niecknig. “The  $\omega \rightarrow \pi^0\gamma^*$  and  $\phi \rightarrow \pi^0\gamma^*$  transition form factors in dispersion theory”. In: *Phys. Rev. D* 86 (2012), p. 054013. DOI: 10.1103/PhysRevD.86.054013. arXiv: 1206.3098 [hep-ph].
- [19] K. Abe et al. “A High Statistics Study of the Decay  $\tau^- \rightarrow \pi^-\pi^0\nu_\tau$ ”. In: *2005 Europhysics Conference on High Energy Physics*. Dec. 2005. arXiv: hep-ex/0512071.
- [20] J. P. Lees et al. “Measurement of the spectral function for the  $\tau^- \rightarrow K^- K_S \nu_\tau$  decay”. In: *Phys. Rev. D* 98.3 (2018), p. 032010. DOI: 10.1103/PhysRevD.98.032010. arXiv: 1806.10280 [hep-ex].
- [21] M. Tanabashi et al. “Review of Particle Physics”. In: *Phys. Rev. D* 98 (3 Aug. 2018), p. 030001. DOI: 10.1103/PhysRevD.98.030001.
- [22] M. Dax, D. Stamen, and B. Kubis. “Dispersive Analysis of the Primakoff Reaction  $\gamma K \rightarrow K\pi$ ”. In: *Eur. Phys. J. C* 81 (2021), p. 221. DOI: 10.1140/epjc/s10052-021-08951-x. arXiv: 2012.04655.
- [23] M. Hoferichter, B. Kubis, and M. Zanke. “Radiative resonance couplings in  $\gamma\pi \rightarrow \pi\pi$ ”. In: *Phys. Rev. D* 96.11 (2017), p. 114016. DOI: 10.1103/PhysRevD.96.114016. arXiv: 1710.00824 [hep-ph].
- [24] M. Hoferichter et al. “Dispersive analysis of the pion transition form factor”. In: *Eur. Phys. J. C* 74 (2014), p. 3180. DOI: 10.1140/epjc/s10052-014-3180-0. arXiv: 1410.4691 [hep-ph].
- [25] E. B. Dally et al. “Direct Measurement of the Negative-Kaon Form Factor”. In: *Phys. Rev. Lett.* 45 (4 July 1980), pp. 232–235. DOI: 10.1103/PhysRevLett.45.232.
- [26] S. R. Amendolia et al. “A Measurement of the Kaon Charge Radius”. In: *Phys. Lett. B* 178 (1986), pp. 435–440. DOI: 10.1016/0370-2693(86)91407-3.
- [27] E. Abouzaid et al. “A measurement of the  $K^0$  charge radius and a  $CP$ -violating asymmetry together with a search for  $CP$ -violating  $E1$  direct photon emission in the rare decay  $K_L \rightarrow \pi^+\pi^-e^+e^-$ ”. In: *Phys. Rev. Lett.* 96 (2006), p. 101801. DOI: 10.1103/PhysRevLett.96.101801. arXiv: hep-ex/0508010.
- [28] A. Lai et al. “Investigation of  $K_{L,S} \rightarrow \pi^+\pi^-e^+e^-$  decays”. In: *Eur. Phys. J. C* 30 (2003), pp. 33–49. DOI: 10.1140/epjc/s2003-01252-y.
- [29] W. R. Molzon et al. “ $K_S$  Regeneration on Electrons From 30-GeV/ $c$  to 100-GeV/ $c$ : A Measurement of the  $K^0$  Radius”. In: *Phys. Rev. Lett.* 41 (1978). [Erratum: *Phys.Rev.Lett.* 41, 1523 (1978), Erratum: *Phys.Rev.Lett.* 41, 1835 (1978)], p. 1213. DOI: 10.1103/PhysRevLett.41.1213.

- [30] H. Foeth et al. “Search for coherent regeneration from electrons - the  $K_0$  charge radius”. In: *Phys. Lett. B* 30 (1969), pp. 276–281. DOI: 10.1016/0370-2693(69)90439-0.
- [31] G. Feinberg. “Electromagnetic Interaction of the Neutral  $K$  Meson”. In: *Phys. Rev.* 109 (1958), pp. 1381–1384. DOI: 10.1103/PhysRev.109.1381.
- [32] R.R. Akhmetshin et al. “Measurement of  $e^+e^- \rightarrow \phi \rightarrow K^+K^-$  cross section with CMD-2 detector at VEPP-2M collider”. In: *Physics Letters B* 669.3 (2008), pp. 217–222. ISSN: 0370-2693. DOI: <https://doi.org/10.1016/j.physletb.2008.09.053>. arXiv: 0804.0178 [hep-ex].
- [33] E. A. Kozyrev et al. “Study of the process  $e^+e^- \rightarrow K^+K^-$  in the center-of-mass energy range 1010–1060 MeV with the CMD-3 detector”. In: *Phys. Lett. B* 779 (2018), pp. 64–71. DOI: 10.1016/j.physletb.2018.01.079. arXiv: 1710.02989 [hep-ex].
- [34] M. N. Achasov et al. “Measurements of the parameters of the  $\phi(1020)$  resonance through studies of the processes  $e^+e^- \rightarrow K^+K^-$ ,  $K_S K_L$ , and  $\pi^+\pi^-\pi^0$ ”. In: *Phys. Rev. D* 63 (2001), p. 072002. DOI: 10.1103/PhysRevD.63.072002. arXiv: hep-ex/0009036.
- [35] J. P. Lees et al. “Precise Measurement of the  $e^+e^- \rightarrow \pi^+\pi^-(\gamma)$  Cross Section with the Initial-State Radiation Method at BABAR”. In: *Phys. Rev. D* 86 (2012), p. 032013. DOI: 10.1103/PhysRevD.86.032013. arXiv: 1205.2228 [hep-ex].
- [36] T. Aoyama et al. “The anomalous magnetic moment of the muon in the Standard Model”. In: *Physics Reports* 887 (2020). The Anomalous Magnetic Moment of the Muon in the Standard Model, pp. 1–166. ISSN: 0370-1573. DOI: <https://doi.org/10.1016/j.physrep.2020.07.006>. arXiv: 2006.04822 [hep-ph].
- [37] R. R. Akhmetshin et al. “Reanalysis of hadronic cross-section measurements at CMD-2”. In: *Phys. Lett. B* 578 (2004), pp. 285–289. DOI: 10.1016/j.physletb.2003.10.108. arXiv: hep-ex/0308008.
- [38] E. A. Kozyrev et al. “Study of the process  $e^+e^- \rightarrow K_S^0 K_L^0$  in the center-of-mass energy range 1004–1060 MeV with the CMD-3 detector at the VEPP-2000  $e^+e^-$  collider”. In: *Phys. Lett. B* 760 (2016), pp. 314–319. DOI: 10.1016/j.physletb.2016.07.003. arXiv: 1604.02981 [hep-ex].
- [39] A. D. Sakharov. “Interaction of an Electron and Positron in Pair Production”. In: *Zh. Eksp. Teor. Fiz.* 18 (1948), pp. 631–635. DOI: 10.1070/PU1991v034n05ABEH002492.
- [40] A. Keshavarzi, D. Nomura, and T. Teubner. “Muon  $g-2$  and  $\alpha(M_Z^2)$ : a new data-based analysis”. In: *Phys. Rev. D* 97.11 (2018), p. 114025. DOI: 10.1103/PhysRevD.97.114025. arXiv: 1802.02995 [hep-ph].
- [41] B. L. Hoid, M. Hoferichter, and B. Kubis. “Hadronic vacuum polarization and vector-meson resonance parameters from  $e^+e^- \rightarrow \pi^0\gamma$ ”. In: *Eur. Phys. J. C* 80.10 (2020), p. 988. DOI: 10.1140/epjc/s10052-020-08550-2. arXiv: 2007.12696 [hep-ph].
- [42] G. D’Agostini. “On the use of the covariance matrix to fit correlated data”. In: *Nucl. Instrum. Meth. A* 346 (1994), pp. 306–311. DOI: 10.1016/0168-9002(94)90719-6.
- [43] M. Hoferichter, B. L. Hoid, and B. Kubis. “Three-pion contribution to hadronic vacuum polarization”. In: *Journal of High Energy Physics* 2019 (Aug. 2019), p. 137. DOI: 10.1007/jhep08(2019)137. arXiv: 1907.01556 [hep-ph].
- [44] R. D. Ball et al. “Fitting Parton Distribution Data with Multiplicative Normalization Uncertainties”. In: *JHEP* 05 (2010), p. 075. DOI: 10.1007/JHEP05(2010)075. arXiv: 0912.2276 [hep-ph].

- 
- [45] R. Dashen. “Chiral  $SU(3) \otimes SU(3)$  as a Symmetry of the Strong Interactions”. In: *Phys. Rev.* 183 (5 July 1969), pp. 1245–1260. DOI: 10.1103/PhysRev.183.1245.
  - [46] C. J. Burden, C. D. Roberts, and M. J. Thomson. “Electromagnetic form-factors of charged and neutral kaons”. In: *Phys. Lett. B* 371 (1996), pp. 163–168. DOI: 10.1016/0370-2693(96)00006-8. arXiv: nucl-th/9511012.



# Acknowledgments

Firstly, I would like to thank Bastian Kubis for supervising my master's thesis. I am grateful that he agreed to take me as his master's student, and for the guidance and support given by him. I did my entire thesis in lockdown, and despite the fact that time was short on his hands, Bastian always took the time to answer my questions and supervise my project.

I thank Dominik Stamen for being my immediate tutor and guiding me throughout my project. He gave me great ideas and helped me with all the issues I had during the whole year of my thesis, answering any question I had without losing patience.

I am grateful to Christoph Hanhart for agreeing to be my second advisor, and the interesting discussions we had regarding my work. I thank him for his support to advance my academic career.

Thanks to Simon Holz for being present at my rehearsal talk and for his suggestions for improvement.

Finally, I thank my family for bringing me up to this stage in my life. They have supported and encouraged me throughout my life.

I also thank my friends who were there for me whenever I needed to take time off.